MODELING OF WAVE PROPAGATION IN TWO-DIMENSIONAL ELASTIC AND POROELASTIC MATERIALS USING FDTD

by

Anuj Guruacharya, B.Eng.

A Thesis Presented in Partial Fulfillment
Of the Requirements for the Degree
Master of Science

COLLEGE OF ENGINEERING AND SCIENCE
LOUISIANA TECH UNIVERSITY

May 2012

LOUISIANA TECH UNIVERSITY

THE GRADUATE SCHOOL

NOVEMBER 29, 2011
Date

We hereby recommend that the thesis prepared under our supervision by

Mr. Anuj Guruacharya, B.Eng.

entitled **Modeling of Wave Propagation in Two-dimensional Elastic and Poroelastic Materials Using FDTD**

be accepted in partial fulfillment of the requirements for the Degree of

Master of Science

Supervisor of Thesis Research

Head of Department
Physics
Department

Recommendation concurred in:

Advisory Committee

Approved:

Director of Graduate Studies

Dean of the College

Approved:

Dean of the Graduate School

GS Form 13
(8/10)

ABSTRACT

Poroelastic materials are solids with fluid filled pores in them. This thesis describes the simulation of the propagation of waves through a two-dimensional geometrical model of a poroelastic and elastic material in the shape of a circular pipe. The poroelastic equations used are obtained from Biot's model of poroelastic materials. The model consists of a numerical solution of a series of partial differential equations. These partial differential equations are solved using the finite-difference time-domain (FDTD) – convolutional perfectly matched layer (CPML) numerical technique. CPML is a boundary condition for the FDTD technique. CPML decreases the reflection in the boundaries of the material. The output data, in the form of images for each time interval, is analyzed to obtain information about the speed of wave propagation in the material. It is shown that the FDTD–CPML technique accurately predicts the nature of the wave propagation in elastic and poroelastic materials using Biot's theory.

APPROVAL FOR SCHOLARLY DISSEMINATION

The author grants to the Prescott Memorial Library of Louisiana Tech University the right to reproduce, by appropriate methods, upon request, any or all portions of this Thesis. It is understood that "proper request" consists of the agreement, on the part of the requesting party, that said reproduction is for his personal use and that subsequent reproduction will not occur without written approval of the author of this Thesis. Further, any portions of the Thesis used in books, papers, and other works must be appropriately referenced to this Thesis.

Finally, the author of this Thesis reserves the right to publish freely, in the literature, at any time, any or all portions of this Thesis.

Author _____

Date _____

TABLE OF CONTENTS

LIST OF FIGURES

LIST OF TABLES

ACKNOWLEDGMENTS

I am thankful to Dr. Neven Simicevic for giving me the initial idea for the project, and Dr. Arun Jaganathan for providing advice on experiments. I am also thankful to Dr. Steve Jones and Dr. John Shaw for the advice on how to proceed with my graduate work.

I would also like to express gratitude towards my co-worker Joseph Snow and the information technology expert, Mr. Michael Bryant. Both of them have helped me in small ways that have amounted to a lot.

CHAPTER 1

INTRODUCTION

Computer simulations have become increasingly important during the latter half of the past century with the advent of high performance computing. In fact, they have given rise to a completely different area of science called computational science, which is distinct from computer science. While computer science deals with how to make computations more efficient, computational sciences deal with using computation in areas of science such as biology and geology. This has led to the rise of fields such as computational biology, computational geology, computational electromagnetics, and computational mechanics. An example of computational electromagnetics is the use of finite difference methods to analyze the propagation of electric and magnetic fields through a medium. Thus, anything to be analyzed or designed is first made into mathematical models and its output is predicted on a computer.

The focus of this thesis is on a subfield of computational mechanics called computational acoustics or computational elastodynamics. Computational acoustics uses computational techniques to tackle problems in mechanical wave propagation through materials with certain mechanical properties. Depending on the frequency of the wave and the mechanical properties of the materials, the problem analyzed can vary from seismic wave propagation in soil [4] to ultrasound wave propagation in bones [12].

A more detailed example can be given of seismic wave propagation. By entering the spatial co-ordinates of the earth (its mountains, buildings, and terrains) into a computer, researchers can simulate how an excitation source in an epicenter of an earthquake propagates through the earth. This will give researchers insight into the destruction caused by the earthquake and the properties of the waves propagated. If the mathematical model that simulates the earthquake is realistic, the conclusions made from the computation of the model will also be realistic.

Besides using a realistic mathematical model, researchers also need to use numerical algorithms that are faster, use less memory, and produce results for a greater range of input values. Genetic algorithms can be used in cases where global optimization is required. Finite difference methods are used in cases where a set of partial differential equations need to be solved.

Thus, the use of realistic mathematical models and the use of superior numerical techniques are the two guiding principles to remember when analyzing or designing a model using the computer. The advancement of these two areas will help researchers obtain data that would sometimes be impossible or too laborious to obtain if done physically on a real system. The data obtained from such computation help in designing better sonar systems, understanding earthquakes, and designing novel devices such as sound vision systems.

The current status of this science finds areas for improvement in two fields: parallel processing and the search for better algorithms to compute mathematical models. First, high performance computing refers to computers being used to perform huge computations and does not address the average desktop computer needs. Parallel

computing, a subfield of high performance computing is a method in which multiple processors are used simultaneously to perform computation. As supercomputers with higher teraflops of computational capacity and higher memory are brought to the market, the development of better computing methods such as parallel computing is becoming equally important to make better use of the resources.

Second, researchers need to improve on the algorithms that are used to computationally represent the mathematics of the model. Various algorithms have come to light from the field of computational biology and computational chemistry. As the volume of data that is to be analyzed becomes larger and the data to be analyzed becomes more complicated, new algorithms need to be designed. An example of such data could be the data obtained from the human gene pool. Unique algorithms are developed from the need to extract valuable information from such data. Thus, there are a lot of research possibilities in these two areas.

This thesis uses the finite-difference time-domain–convolutional perfectly matched layer (FDTD-CPML) computational algorithm to simulate wave propagation in two-dimensional solids that have pores on them. Examples of such materials are rocks, soil, cement, ceramics, and biological tissues, such as bones and wood. A realistic two-dimensional model is used in this thesis to simulate the propagation of mechanical waves in such media. The model widely used model is called Biot's theory of wave propagation in poroelastic solid. This model was proposed by M. A. Biot in 1941 [26]. To compute this model, the FDTD-CPML algorithm is widely used. This algorithm was introduced by Rodney and Gedney in 2000 [8]. Finite-difference time-domain (FDTD) is a computational technique to solve partial differential equations. Convolutional perfectly

matched layer (CPML) is a specific FDTD technique in which the boundary of the system simulated is assumed to be perfectly matched. Thus an efficient computational implementation of the most realistic poroelastic wave propagation model has been pursued in this thesis.

CHAPTER 2

LITERATURE SURVEY

Real physical media are three-dimensional and exhibit complex topologies. They may include a mixture of gases, solids, and liquids. Fluid saturated media is one type of mixture. If the fluid resides in the pores of a solid, the solid is known as a poroelastic solid. Many natural materials such as soil and bones are poroelastic solids. The analysis of waves propagating in poroelastic solids provide better insight for earthquake impact analysis, exploration of natural resources, detection of voids in soil, and medical imaging of bones.

The effect of pore pressure, fluid viscosity, porosity, permeability, and slip velocity between phases can be taken into account in models of poroelastic solids. These additional parameters allow the coupling of propagated waves to the local diffusion of viscous fluids. The modeling of land mines buried under soil or the modeling of bones to detect various diseases such as osteoporosis and cancer requires the use of poroelastic models. Diseased bones and cancerous tissues have a different poroelastic character than healthy bones and tissues [11]. Using this difference, researchers can diagnose the disease and determine which part of the body is affected by the disease.

The work done by Martin and Komatitsch [7] has served as a guiding light in this project. The FDTD grids used in this project were originally proposed by them. Below

will be described in detail the wave equations for elastic mechanics and poroelastic mechanics; their corresponding FDTD solutions; and their corresponding FDTD-CPML implementation.

2.1 Mechanical Wave Propagation in Elastic Solids

The wave equations of mechanics are more complicated than the wave equations of electromagnetism because of the tensor nature of the stress which is one of the two variables in a mechanical wave equation. By comparing the structure of different physical equations, a great amount of knowledge about wave mechanics can be derived. No matter what kind of mathematical representation the variable has, they all follow the same structure of partial differential equations (PDEs) for waves. Such equations are second order differential in space and second order differential in time. If the PDE is first order differential in space and second order differential in time, it is a diffusion system rather than a wave propagation system.

2.1.1 Elastic Waves in Pressure Velocity Formulation

In Equation 2.1, the elastic wave equation is presented where pressure is a scalar and velocity is a vector. So there will be a difference in the number of equations from an electromagnetic wave in which both variables are vectors, as shown in Equation 2.1.

$$\frac{\partial v}{\partial t} = -\frac{1}{\rho}\nabla p, \tag{2.1.a}$$

$$\frac{\partial p}{\partial t} = -\rho c^2 \, \nabla \cdot v. \tag{2.1.b}$$

In Equation 2.1,

ρ = density of the solid, a scalar constant,

c = speed of mechanical wave in the solid, a scalar constant,

p = pressure, a scalar variable, and

v = velocity, a vector variable.

Equation 2.1 can be expanded into different scalar equations depending on the dimension of the problem. Table 1 gives the number of scalar equations of the different variables in Equation 2.1 for different dimensions.

Table 1 Number of scalar equations expandable from Equation 2.1

	Velocity	Pressure
One-dimensional	1	1
Two-dimensional	2	1
Three-dimensional	3	1

2.1.1.1 *One-dimensional elastic waves in pressure velocity formulation*

For one dimension, Equation 2.1 can be expanded to one scalar equation for v_x and one scalar equation for p, as shown in Equation 2.2.

$$\frac{\partial v_x}{\partial t} = -\frac{1}{\rho}\frac{\partial p}{\partial x}, \tag{2.2.a}$$

$$\frac{\partial p}{\partial t} = -\rho c^2 \frac{\partial v_x}{\partial x}. \tag{2.2.b}$$

2.1.1.2 *Two-dimensional elastic waves in pressure velocity formulation*

For two dimensions, the expanded equation contains two scalar equations for v and one scalar equation for p, as shown in Equation 2.3.

$$\frac{\partial v_x}{\partial t} = -\frac{1}{\rho}\frac{\partial p}{\partial x}, \tag{2.3.a}$$

$$\frac{\partial v_y}{\partial t} = -\frac{1}{\rho}\frac{\partial p}{\partial y}, \tag{2.3.b}$$

$$\frac{\partial p}{\partial t} = -\rho c^2 \left(\frac{\partial v_x}{\partial x} + \frac{\partial v_y}{\partial y}\right). \tag{2.3.c}$$

Here, v_x and v_y are the spatial components of velocity. Since pressure is a scalar, only one equation is obtained for a change in pressure with respect to time. Since velocity is a vector, two equations are obtained for change in velocity with respect to time.

2.1.1.3 *Three-dimensional elastic waves in pressure velocity formulation*

For three dimensions, the expanded equation contains three scalar equations for v and one scalar equation for p, as shown in Equation 2.4.

$$\frac{\partial v_x}{\partial t} = -\frac{1}{\rho}\frac{\partial p}{\partial x}, \tag{2.4.a}$$

$$\frac{\partial v_y}{\partial t} = -\frac{1}{\rho}\frac{\partial p}{\partial y}, \tag{2.4.b}$$

$$\frac{\partial v_z}{\partial t} = -\frac{1}{\rho}\frac{\partial p}{\partial z}, \tag{2.4.c}$$

$$\frac{\partial p}{\partial t} = -\rho c^2 \left(\frac{\partial v_x}{\partial x} + \frac{\partial v_y}{\partial y} + \frac{\partial v_z}{\partial z}\right). \tag{2.4.d}$$

Here, v_x, v_y, and v_z are the three spatial components of velocity. Since velocity is a vector, three separate equations are obtained for change in velocity with respect to time. Since pressure is a scalar, only one equation is obtained for change in pressure with respect to time.

2.1.2 Elastic Waves in Stress Velocity Formulation

A stress and velocity formulation is more realistic because stress is a tensor quantity and thus gives more information about the nature of wave propagation. To get a more accurate picture of wave propagation in solids, a stress and velocity formulation of the model is needed, as shown in Equation 2.5.

$$\nabla \cdot \bar{\bar{\sigma}} = \rho \frac{\partial v}{\partial t}, \tag{2.5.a}$$

$$\frac{\partial \bar{\bar{\sigma}}}{\partial t} = \bar{\bar{\bar{\bar{c}}}} : \nabla v . \tag{2.5.b}$$

In Equation 2.8,

$\bar{\bar{\sigma}} = \text{stress, a tensor variable of order 2,}$

$v = \text{velocity, a vector variable,}$

$\rho = \text{density, a scalar constant, and}$

$\bar{\bar{\bar{\bar{c}}}} = \text{compliance matrix, a tensor constant of order 4.}$

Here, a contraction process is performed between the compliance matrix and the differential of the velocity. The symbol ∇ represents the nabla operator which operates on both stress and velocity. According to the dimension of the wave, the velocity vector can be broken down into its spatial components: v_x, v_y, and v_z. Table 2 gives the number of scalar equations of the different variables in Equation 2.8 for different dimensions.

Table 2 Number of scalar equations expandable from Equation 2.5

	Stress	Velocity
One-dimensional	1	1
Two-dimensional	3	2
Three-dimensional	6	3

2.1.2.1 *One-dimensional elastic waves in stress velocity formulation*

For one dimension, the expanded equation contains one scalar equation for velocity and one scalar equation for stress where K is the bulk modulus of the solid and is a part of the compliance matrix while ρ is the density of the solid, as shown in Equation 2.6.

$$\frac{\partial v_x}{\partial t} = -\frac{1}{\rho}\frac{\partial \sigma_x}{\partial x}, \tag{2.6.a}$$

$$\frac{\partial \sigma_x}{\partial t} = -K\frac{\partial v_x}{\partial x}. \tag{2.6.b}$$

2.1.2.2 *Two-dimensional elastic waves in stress velocity formulation*

In real mechanical systems, one dimension is not enough to describe a wave. For two dimensions, the expanded equation contains two scalar equations for velocity and three scalar equations for stress, where λ is wavelength of the wave in the solid and μ is permeability of the wave in the solid, as shown in Equation 2.7.

$$\rho \frac{\partial v_x}{\partial t} = \frac{\partial \sigma_{xx}}{\partial x} + \frac{\partial \sigma_{xy}}{\partial y}, \tag{2.7.a}$$

$$\rho \frac{\partial v_y}{\partial t} = \frac{\partial \sigma_{xy}}{\partial x} + \frac{\partial \sigma_{yy}}{\partial y}, \tag{2.7.b}$$

$$\frac{\partial \sigma_{xx}}{\partial t} = (\lambda + 2\mu) \frac{\partial v_x}{\partial x} + \lambda \frac{\partial v_y}{\partial y}, \tag{2.7.c}$$

$$\frac{\partial \sigma_{yy}}{\partial t} = (\lambda + 2\mu) \frac{\partial v_y}{\partial y} + \lambda \frac{\partial v_x}{\partial x}, \tag{2.7.d}$$

$$\frac{\partial \sigma_{xy}}{\partial t} = \mu \frac{\partial v_y}{\partial x} + \mu \frac{\partial v_x}{\partial y} . \tag{2.7.e}$$

The terms $\sigma_{xy}$and σ_{yx} are considered equal, so one of the terms is neglected. The compliance matrix is a rank four tensor of order two, so there are 16 individual values inside the compliance matrix. The compliance matrix when expanded gives rise to the Lame's parameters. The constants represented by $(\lambda + 2\mu)$, μ, and λ are Lame's parameters [5]. These parameters depend on the type of material.

2.1.2.3 *Three-dimensional elastic waves in stress velocity formulation*

For three dimensions, the expanded equation contains three scalar equations for velocity and six scalar equations for stress, as shown in Equation 2.8.

$$\rho \frac{\partial v_x}{\partial t} = \frac{\partial \sigma_{xx}}{\partial x} + \frac{\partial \sigma_{xy}}{\partial y} + \frac{\partial \sigma_{xz}}{\partial z}, \tag{2.8.a}$$

$$\rho \frac{\partial v_y}{\partial t} = \frac{\partial \sigma_{xy}}{\partial x} + \frac{\partial \sigma_{yy}}{\partial y} + \frac{\partial \sigma_{yz}}{\partial z}, \tag{2.8.b}$$

$$\rho \frac{\partial v_z}{\partial t} = \frac{\partial \sigma_{xz}}{\partial x} + \frac{\partial \sigma_{yz}}{\partial y} + \frac{\partial \sigma_{zz}}{\partial z}, \tag{2.8.c}$$

$$\frac{\partial \sigma_{xx}}{\partial t} = (\lambda + 2\mu)\frac{\partial v_x}{\partial x} + \lambda \frac{\partial v_y}{\partial y} + \lambda \frac{\partial v_z}{\partial z}, \tag{2.8.d}$$

$$\frac{\partial \sigma_{yy}}{\partial t} = \lambda \frac{\partial v_x}{\partial x} + (\lambda + 2\mu)\frac{\partial v_y}{\partial y} + \lambda \frac{\partial v_z}{\partial z}, \tag{2.8.e}$$

$$\frac{\partial \sigma_{zz}}{\partial t} = \lambda \frac{\partial v_x}{\partial x} + \lambda \frac{\partial v_y}{\partial y} + (\lambda + 2\mu)\frac{\partial v_z}{\partial z}, \tag{2.8.f}$$

$$\frac{\partial \sigma_{yz}}{\partial t} = \mu \frac{\partial v_y}{\partial z} + \mu \frac{\partial v_z}{\partial y}, \tag{2.8.g}$$

$$\frac{\partial \sigma_{xz}}{\partial t} = \mu \frac{\partial v_x}{\partial z} + \mu \frac{\partial v_z}{\partial x}, \tag{2.8.h}$$

$$\frac{\partial \sigma_{xy}}{\partial t} = \mu \frac{\partial v_x}{\partial y} + \mu \frac{\partial v_y}{\partial x}. \tag{2.8.i}$$

The terms for σ_{xy} and σ_{yx}; σ_{xz} and σ_{zx} ; σ_{yz} and σ_{zy} are considered equal so only one of the terms has been used in Equation 2.8. The compliance matrix is a rank four tensor of order three, so there are 81 individual values inside the compliance matrix. However, not all the values of the compliance matrix are unique, so Lame's parameters are used to fill up the values inside the compliance matrix that are common.

2.2 Mechanical Wave Propagation in Poroelastic Solid

Poroelastic materials have similar equations with the addition of extra equations from the Reynolds Transport theorem equations, which form the basic equations of fluid mechanics. Biot's theory [28][31][32], which was first given by M. Biot, has been widely

used to explain wave propagation in porous solid. Biot's equations of the linear theory of poroelasticity are derived from the following equations:

- Equations of linear elasticity for the solid matrix,
- Navier–Stokes equations for the viscous fluid, and
- Darcy's equations for the flow of fluid through the porous matrix.

Since a poroelastic material has both fluid and solid components in it, a model of wave propagation in poroelastic solid media contains more equations than a model of wave propagation in elastic solid media. There are four variables in the model. The four variables are:

- Stress tensor in solid , $\bar{\bar{\sigma}}$,
- Velocity vector in solid, $\bar{v}^s$,
- Pressure scalar in fluid, P^f, and
- Velocity vector in fluid, $\bar{v}^f$.

The differential form of the wave propagation in a porous solid is given in Equation 2.9 [29].

$$\left(\rho_w \rho - \rho_f^2\right) \frac{\partial v^s}{\partial t} = \rho_w \nabla \cdot \bar{\bar{\sigma}} + \rho_f \nabla P^f + \rho K v^f, \tag{2.9.a}$$

$$\left(\rho_w \rho - \rho_f^2\right) \frac{\partial v^f}{\partial t} = -\rho_f \dot{\nabla} \bar{\bar{\sigma}} - \rho \nabla P^f - \rho_f K v^f, \tag{2.9.b}$$

$$\frac{\partial \bar{\bar{\sigma}}}{\partial t} = \bar{\bar{\bar{C}}} : \nabla v^s - \alpha \partial_t P^f I, \tag{2.9.c}$$

$$\frac{\partial P^f}{\partial t} = -\alpha M \nabla \cdot v^s - M \nabla \cdot v^f. \tag{2.9.d}$$

The following constants are included in Equation 2.9:

ρ_w = apparent density of the porous solid, a scalar,

ρ = density of the solid component of the porous solid, a scalar,

ρ_f = density of the fluid component of the porous solid, a scalar,

α = porosity of the porous solid, a scalar,

M = bulk modulus of the porous solid, a scalar,

$\overline{\overline{\overline{C}}}$ = compliance matrix of the porous solid, a tensor of rank 4, and

K = damping viscous term, a scalar.

Depending on the dimension, Equation 2.9 can be expanded into different scalar equations. Table 3 gives the number of scalar equations of the different variables in Equation 2.9 for different dimensions.

Table 3 Number of scalar equations expandable from Equation 2.9

	Velocity in fluid	Velocity in solid	Pressure in fluid	Stress in solid
One-dimensional	1	1	1	1
Two-dimensional	2	2	1	3
Three-dimensional	3	3	1	6

2.2.1 One-dimensional Poroelastic Waves

For one dimension, the expanded equation contains one scalar equation for v_s, one scalar equation for v_f, one scalar equation for σ, and one scalar equation for P_f, as shown in Equation 2.10.

$$\left(\rho_w\rho - \rho_f^2\right)\frac{\partial v_x^s}{\partial t} = \rho_w\left(\frac{\partial \sigma_{xx}}{\partial x}\right) + \rho_f\frac{\partial P^f}{\partial x} + \rho K v_x^f, \quad (2.10.a)$$

$$\left(\rho_w\rho - \rho_f^2\right)\frac{\partial v_x^f}{\partial t} = -\rho_f\left(\frac{\partial \sigma_{xx}}{\partial x}\right) - \rho\frac{\partial P^f}{\partial x} - \rho_f K v_x^f, \quad (2.10.b)$$

$$\frac{\partial \sigma_{xx}}{\partial t} = (\lambda_s + 2\mu)\frac{\partial v_x}{\partial x} + -\alpha\frac{\partial P^f}{\partial t}, \quad (2.10.c)$$

$$\frac{\partial P^f}{\partial t} = -\alpha M\left(\frac{\partial v_x^s}{\partial x} + \frac{\partial v_y^s}{\partial y}\right) - M\left(\frac{\partial v_x^f}{\partial x} + \frac{\partial v_y^f}{\partial y}\right). \quad (2.10.d)$$

The compliance matrix is a tensor of rank four and order one, so it has one component in it only. That component would be the constant represented by $\lambda_s + 2\mu$, which is one of Lame's parameters [30]. In Equation 2.10, σ_{xx} is the only component of stress and v_x is the only component of velocity present.

2.2.2 Two-dimensional Poroelastic Waves

Two dimensional poroelastic waves are easier to analyze than three dimensional poroelastic waves. They simulate the phenomena without sarificing the number of equations used to describe wave propagation. For two dimensions, the expanded equation contains two scalar equations for v_s, two scalar equations for v_f, three scalar equations for σ, and one scalar equation for P_f, as shown in Equation 2.11.

$$\left(\rho_w\rho - \rho_f^2\right)\frac{\partial v_x^s}{\partial t} = \rho_w\left(\frac{\partial \sigma_{xx}}{\partial x} + \frac{\partial \sigma_{xy}}{\partial y}\right) + \rho_f\frac{\partial P^f}{\partial x} + \rho K v_x^f, \quad (2.11.a)$$

$$\left(\rho_w\rho - \rho_f^2\right)\frac{\partial v_y^s}{\partial t} = \rho_w\left(\frac{\partial \sigma_{xy}}{\partial x} + \frac{\partial \sigma_{yy}}{\partial y}\right) + \rho_f\frac{\partial P^f}{\partial y} + \rho K v_y^f, \quad (2.11.b)$$

$$\left(\rho_w\rho - \rho_f^2\right)\frac{\partial v_x^f}{\partial t} = -\rho_f\left(\frac{\partial \sigma_{xx}}{\partial x} + \frac{\partial \sigma_{xy}}{\partial y}\right) - \rho\frac{\partial P^f}{\partial x} - \rho_f K v_x^f, \qquad (2.11.c)$$

$$\left(\rho_w\rho - \rho_f^2\right)\frac{\partial v_y^f}{\partial t} = -\rho_f\left(\frac{\partial \sigma_{xy}}{\partial x} + \frac{\partial \sigma_{yy}}{\partial y}\right) - \rho\frac{\partial P^f}{\partial y} - \rho_f K v_y^f, \qquad (2.11.d)$$

$$\frac{\partial \sigma_{xx}}{\partial t} = (\lambda_s + 2\mu)\frac{\partial v_x}{\partial x} + \lambda_s\frac{\partial v_y}{\partial y} - \alpha\frac{\partial P^f}{\partial t}, \qquad (2.11.e)$$

$$\frac{\partial \sigma_{yy}}{\partial t} = \lambda_s\frac{\partial v_x}{\partial x} + (\lambda_s + 2\mu)\frac{\partial v_y}{\partial y} - \alpha\frac{\partial P^f}{\partial t}, \qquad (2.11.f)$$

$$\frac{\partial \sigma_{xy}}{\partial t} = \mu\frac{\partial v_x}{\partial y} + \mu\frac{\partial v_y}{\partial x}, \qquad (2.11.g)$$

$$\frac{\partial P^f}{\partial t} = -\alpha M\left(\frac{\partial v_x^s}{\partial x} + \frac{\partial v_y^s}{\partial y}\right) - M\left(\frac{\partial v_x^f}{\partial x} + \frac{\partial v_y^f}{\partial y}\right). \qquad (2.11.h)$$

The compliance matrix is a rank four tensor of order two, so there are 2^4, that is 16, individual values inside the C matrix. The compliance matrix when expanded gives rise to the Lame's parameters. So the constants $(\lambda + 2\mu)$, μ, and λ are all Lame's parameters. The scalars σ_{xx}, σ_{xy}, and σ_{yy} are components of the sress tensor.

2.2.3 Three-dimensional Poroelastic Waves

Real systems are three dimensional and must include additional equations to accurately simulate waves in such systems. For three dimensions, the expanded equation contains 13 equations in total as given below:

- Six scalar equations for stress in solid,
- One scalar equation for pressure in fluid,

- Three scalar equations for velocity in solid, and
- Three scalar equations for velocity in fluid.

The three scalar equations for velocity in solid are shown in Equation 2.12.

$$\left(\rho_w\rho - \rho_f^2\right)\frac{\partial v_x^s}{\partial t} = \rho_w\left(\frac{\partial \sigma_{xx}}{\partial x} + \frac{\partial \sigma_{xy}}{\partial y} + \frac{\partial \sigma_{xz}}{\partial z}\right) + \rho_f\frac{\partial P^f}{\partial x} + \rho K v_x^f, \quad (2.12.a)$$

$$\left(\rho_w\rho - \rho_f^2\right)\frac{\partial v_y^s}{\partial t} = \rho_w\left(\frac{\partial \sigma_{xy}}{\partial x} + \frac{\partial \sigma_{yy}}{\partial y} + \frac{\partial \sigma_{yz}}{\partial z}\right) + \rho_f\frac{\partial P^f}{\partial y} + \rho K v_y^f, \quad (2.12.b)$$

$$\left(\rho_w\rho - \rho_f^2\right)\frac{\partial v_z^s}{\partial t} = \rho_w\left(\frac{\partial \sigma_{xz}}{\partial x} + \frac{\partial \sigma_{yz}}{\partial y} + \frac{\partial \sigma_{zz}}{\partial z}\right) + \rho_f\frac{\partial P^f}{\partial z} + \rho K v_z^f. \quad (2.12.c)$$

The scalar equation for pressure in fluid is shown in Equation 2.13.

$$\frac{\partial P^f}{\partial t} = -\alpha M\left(\frac{\partial v_x^s}{\partial x} + \frac{\partial v_y^s}{\partial y} + \frac{\partial v_z^s}{\partial z}\right) - M\left(\frac{\partial v_x^f}{\partial x} + \frac{\partial v_y^f}{\partial y} + \frac{\partial v_z^f}{\partial z}\right). \quad (2.13)$$

The three scalar equations for velocity in fluid are shown in Equation 2.14.

$$\left(\rho_w\rho - \rho_f^2\right)\frac{\partial v_x^f}{\partial t} = -\rho_f\left(\frac{\partial \sigma_{xx}}{\partial x} + \frac{\partial \sigma_{xy}}{\partial y} + \frac{\partial \sigma_{xz}}{\partial z}\right) - \rho\frac{\partial P^f}{\partial x} - \rho_f K v_x^f, \quad (2.14.a)$$

$$\left(\rho_w\rho - \rho_f^2\right)\frac{\partial v_y^f}{\partial t} = -\rho_f\left(\frac{\partial \sigma_{xy}}{\partial x} + \frac{\partial \sigma_{yy}}{\partial y} + \frac{\partial \sigma_{yz}}{\partial z}\right) - \rho\frac{\partial P^f}{\partial y} - \rho_f K v_y^f, \quad (2.14.b)$$

$$\left(\rho_w\rho - \rho_f^2\right)\frac{\partial v_z^f}{\partial t} = -\rho_f\left(\frac{\partial \sigma_{xz}}{\partial x} + \frac{\partial \sigma_{yz}}{\partial y} + \frac{\partial \sigma_{zz}}{\partial z}\right) - \rho\frac{\partial P^f}{\partial z} - \rho_f K v_z^f. \quad (2.14.c)$$

The six scalar equations for stress in solid are shown in Equation 2.15.

$$\frac{\partial \sigma_{xx}}{\partial t} = (\lambda_s + 2\mu)\frac{\partial v_x}{\partial x} + \lambda_s\frac{\partial v_y}{\partial y} + \lambda_s\frac{\partial v_z}{\partial z} - \alpha\frac{\partial P^f}{\partial t}, \quad (2.15.a)$$

$$\frac{\partial \sigma_{yy}}{\partial t} = \lambda_s\frac{\partial v_x}{\partial x} + (\lambda_s + 2\mu)\frac{\partial v_y}{\partial y} + \lambda_s\frac{\partial v_z}{\partial z} - \alpha\frac{\partial P^f}{\partial t}, \quad (2.15.b)$$

$$\frac{\partial \sigma_{zz}}{\partial t} = \lambda_s\frac{\partial v_x}{\partial x} + \lambda_s\frac{\partial v_y}{\partial y} + (\lambda_s + 2\mu)\frac{\partial v_z}{\partial z} - \alpha\frac{\partial P^f}{\partial t}, \quad (2.15.c)$$

$$\frac{\partial \sigma_{yz}}{\partial t} = \mu \frac{\partial v_y}{\partial z} + \mu \frac{\partial v_z}{\partial y}, \quad (2.15.d)$$

$$\frac{\partial \sigma_{xz}}{\partial t} = \mu \frac{\partial v_x}{\partial z} + \mu \frac{\partial v_z}{\partial x}, \quad (2.15.e)$$

$$\frac{\partial \sigma_{xy}}{\partial t} = \mu \frac{\partial v_x}{\partial y} + \mu \frac{\partial v_y}{\partial x}. \quad (2.15.f)$$

The compliance matrix is a rank four tensor of order three, so it contains 3^4, that is 81, individual values. The compliance matrix when expanded, gives rise to the Lame's parameters. Other constants of the equations are not affected by the addition of an extra dimension because the other constants are scalars. Thus, the waves in poroelastic solids are more complicated because they contain equations from both solid mechanics and fluid mechanics.

2.3 Numerical Methods to Solve PDE

Various numerical methods have been developed for numerical solutions of partial differential equations, such as finite element methods, finite volume methods, and finite difference methods. However, finite difference methods are more suitable for simulation of wave propagation because of the inclusion of a time domain [3]. They are thus called the finite-difference time-domain (FDTD) methods.

If the wave equations presented in the above sections are changed into FDTD form, the values of all the variables in the two-dimensional or three-dimensional grid of the equations can be obtained. When solving differential equations using the FDTD technique, it is usually wise to divide the domain into grids and then find the value of the electric field and magnetic field, or velocity and pressure at individual points in the grid.

The wave equations presented in the previous section will be presented in this section in FDTD grid format and in the form of FDTD equations. This method of discretizing the equations is known as the Yee algorithm for FDTD which was first proposed by Kane Yee [1] in 1966 in a paper in *IEEE Transactions on Antennas and Propagation*. The descriptor "Finite-difference time-domain" and its corresponding "FDTD" acronym were originated by Allen Taflove [2] in a 1980 paper in *IEEE Transactions on Electromagnetic Compatibility*. It was Allen Taflove who showed the efficiency of the Yee algorithm in solving coupled PDEs.

2.3.1 Elastic Wave Equation Computation Using FDTD without Boundary Layers in Pressure and Velocity Formulation

2.3.1.1 *One-dimensional elastic wave equation computation using FDTD in pressure and velocity formulation*

For one dimension, the FDTD grid is similar to the Yee grid of the electromagnetic wave. In Figure 1, the pressure term is considered to have integer values of position (*m)* and integer values of position (*q)* in the grid.

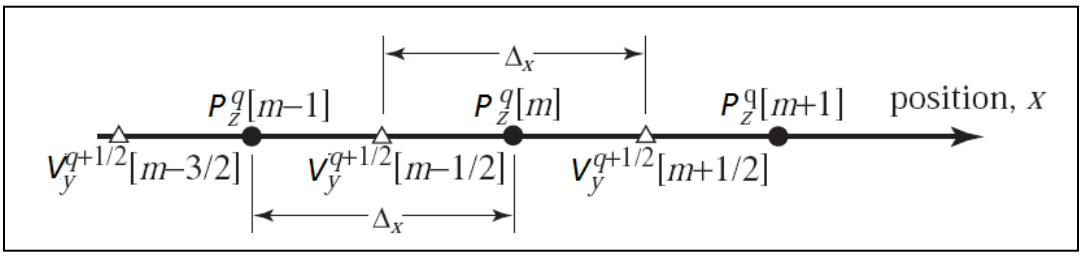

Figure 1 One-dimensional FDTD grid for velocity and pressure in elastic solids

Using the FDTD grid in Figure 1, equations for velocity and pressure can be formulated using the FDTD central difference formula, as shown in Equation 2.16.

$$v_{x_{m+\frac{1}{2}}}^{q+\frac{1}{2}} = v_{x_{m+\frac{1}{2}}}^{q-\frac{1}{2}} - \frac{1}{\rho}\frac{\partial t}{\partial x}\left(p_{m+1}^{q} - p_{m}^{q}\right), \tag{2.16.a}$$

$$p_{m}^{q+1} = p_{m}^{q} - K\frac{\partial t}{\partial x}\left(v_{x_{m+\frac{1}{2}}}^{q+\frac{1}{2}} - v_{x_{m-\frac{1}{2}}}^{q+\frac{1}{2}}\right). \tag{2.16.b}$$

In Equation 2.16, *m* is the spatial index and *q* is the temporal index. The *v* term has been offset one half in time and one half in space. A program can now be written which loops through these equations starting from the boundary conditions from where the values of the *p* and *v* for all the regions of the mesh can be found.

2.3.1.2 *Two-dimensional elastic wave equation computation using FDTD in pressure and velocity formulation*

The pressure term will be considered to be the term with *m* and *n* discrete values while the terms v_x and v_y will be offset one half in space and time from *P*. The grid for the two-dimensional case is shown in Figure 2.

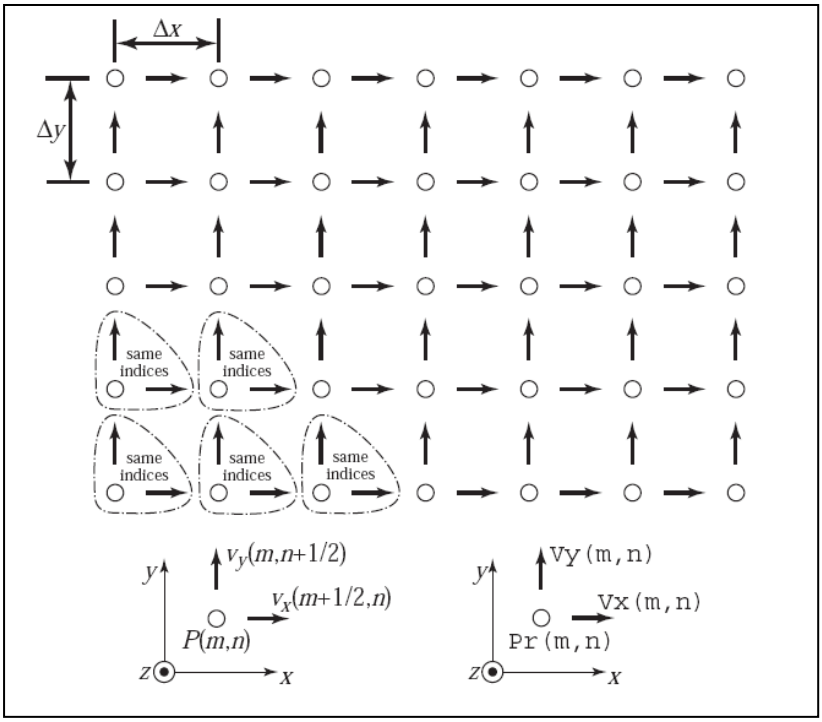

Figure 2 Two-dimensional FDTD grid for pressure and velocity in elastic solids

From the FDTD grid in Figure 2, the FDTD equations are obtained as shown in Equation 2.17.

$$P_{m,n}^{q} = P_{m,n}^{q-1} - K\frac{\partial t}{\partial x}\left(v_{x_{m+\frac{1}{2},n}}^{q-\frac{1}{2}} - v_{x_{m-\frac{1}{2},n}}^{q-\frac{1}{2}} + v_{y_{m,n+\frac{1}{2}}}^{q-\frac{1}{2}} - v_{y_{m,n-\frac{1}{2}}}^{q-\frac{1}{2}} \right), \quad (2.17.a)$$

$$v_{x_{m+\frac{1}{2},n}}^{q+\frac{1}{2}} = v_{x_{m+\frac{1}{2},n}}^{q-\frac{1}{2}} - \frac{1}{\rho}\frac{\partial t}{\partial x}\left(P_{m+1,n}^{q} - P_{m,n}^{q} \right), \quad (2.17.b)$$

$$v_{y_{m,n+\frac{1}{2}}}^{q+\frac{1}{2}} = v_{y_{m,n+\frac{1}{2}}}^{q-\frac{1}{2}} - \frac{1}{\rho}\frac{\partial t}{\partial x}\left(P_{m,n+1}^{q} - P_{m,n}^{q} \right). \quad (2.17.c)$$

2.3.1.3 *Three-dimensional elastic wave equation computation using FDTD in pressure and velocity formulation*

For three-dimensional cases, with pressure at the center of the Yee cell, and velocity at the sides, the Yee cell shown in Figure 3 is obtained. The variables *m*, *n*, and *p*

represent, respectively, the *x*, *y*, and *z* spatial co-ordinates. The variable *q* represents the temporal index.

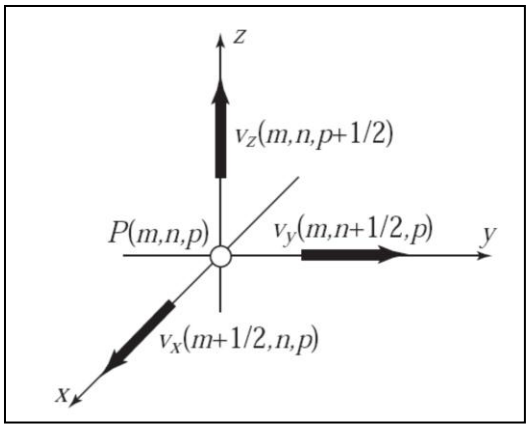

Figure 3 Three-dimensional FDTD cell for pressure and velocity in elastic solids

The FDTD equations obtained from the grid in Figure 3 are given in Equation 2.18.

$$P^{q}_{m,n,p} = P^{q-1}_{m,n,p} - K\frac{\partial t}{\partial x}\left(v_{x}^{q-\frac{1}{2}}{}_{m+\frac{1}{2},n,p} - v_{x}^{q-\frac{1}{2}}{}_{m-\frac{1}{2},n,p} + v_{y}^{q-\frac{1}{2}}{}_{m,n+\frac{1}{2},p} - v_{y}^{q-\frac{1}{2}}{}_{m,n-\frac{1}{2},p} + v_{z}^{q-\frac{1}{2}}{}_{m,n,p+\frac{1}{2}} - v_{z}^{q-\frac{1}{2}}{}_{m.n.p-\frac{1}{2}} \right), \quad (2.18.a)$$

$$v_{x}^{q+\frac{1}{2}}{}_{m+\frac{1}{2},n,p} = v_{x}^{q-\frac{1}{2}}{}_{m+\frac{1}{2},n,p} - \frac{1}{\rho}\frac{\partial t}{\partial x}\left(P^{q}_{m+1,n,p} - P^{q}_{m,n,p} \right), \quad (2.18.b)$$

$$v_{y}^{q+\frac{1}{2}}{}_{m,n+\frac{1}{2},p} = v_{y}^{q-\frac{1}{2}}{}_{m,n+\frac{1}{2},p} - \frac{1}{\rho}\frac{\partial t}{\partial x}\left(P^{q}_{m,n+1,p} - P^{q}_{m,n,p} \right), \quad (2.18.c)$$

$$v_{z}^{q+\frac{1}{2}}{}_{m,n,p+\frac{1}{2}} = v_{z}^{q-\frac{1}{2}}{}_{m,n,p+\frac{1}{2}} - \frac{1}{\rho}\frac{\partial t}{\partial x}\left(P^{q}_{m,n,p+1} - P^{q}_{m,n,p} \right). \quad (2.18.d)$$

2.3.2 Elastic Wave Equation Computation Using FDTD without Boundary Layers in Stress and Velocity Formulation

2.3.2.1 *One-dimensional elastic wave equation computation using FDTD in stress and velocity formulation*

For a one-dimensional case, the grid and the equations for a stress and velocity formulation are going to be the same as in a one-dimensional case with pressure and velocity formulation. In Figure 4, velocity, $v_x(m)$, will be kept at the origin rather than pressure.

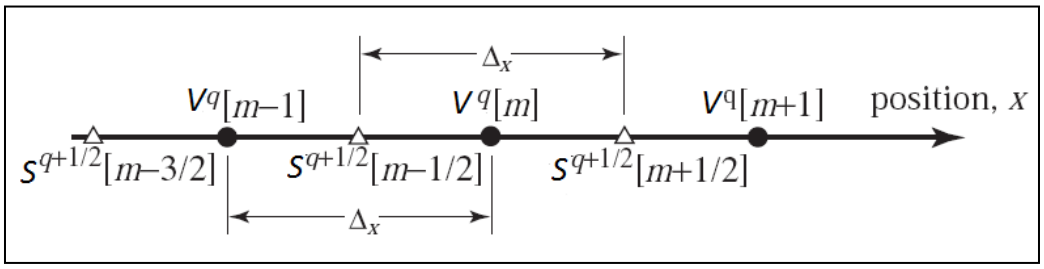

Figure 4 One-dimensional FDTD grid for velocity and stress in elastic solids

Using the FDTD grid in Figure 4, the FDTD equations shown in Equation 2.19 are obtained.

$$v_{x_m}^{q+\frac{1}{2}} = v_{x_m}^{q-\frac{1}{2}} - \frac{1}{\rho}\frac{\partial t}{\partial x}\left(\sigma_{m+\frac{1}{2}}^{q} - \sigma_{m-\frac{1}{2}}^{q}\right), \tag{2.19.a}$$

$$\sigma_{m+\frac{1}{2}}^{q+1} = \sigma_{m+\frac{1}{2}}^{q} - K\frac{\partial t}{\partial x}\left(v_{x_m}^{q+\frac{1}{2}} - v_{x_{m-1}}^{q+\frac{1}{2}}\right). \tag{2.19.b}$$

2.3.2.2 *Two-dimensional elastic wave equation computation using FDTD in stress and velocity formulation*

For a two-dimensional case, the FDTD cell shown in Figure 5 can be used.

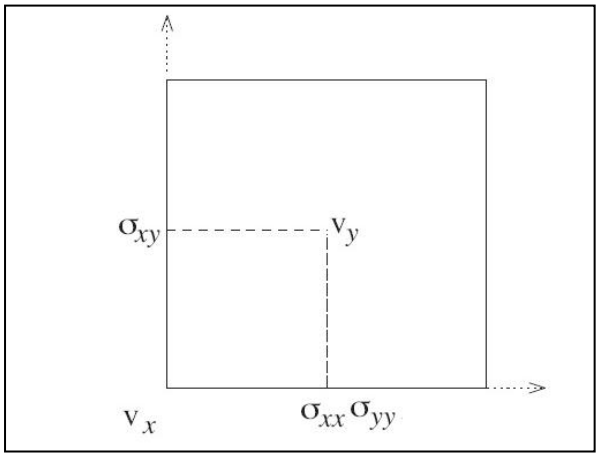

Figure 5 Two-dimensional FDTD cell for pressure and velocity in elastic materials

In Figure 5, the velocity, v_x, is at the center of the cell with co-ordinates *(m, n)*. The variable *q* represents the temporal index. The temporal index of velocity is offset by a value of $q + ½$ and temporal index of pressure is offset by a value of $q + 1$. From Figure 5, the FDTD equations for stress shown in Equation 2.20 are obtained.

$$\sigma_{xx}{}^{q}_{m+\frac{1}{2},n} = \sigma_{xx}{}^{q-1}_{m+\frac{1}{2},n} + \frac{\partial t}{\partial x}\left\{(\lambda+2\mu)\left(v_{x_{m,n}}^{q-\frac{1}{2}} - v_{x_{m-1,n}}^{q-\frac{1}{2}}\right) + \lambda\left(v_{y_{m+\frac{1}{2},n+\frac{1}{2}}}^{q-\frac{1}{2}} - v_{y_{m+\frac{1}{2},n-\frac{1}{2}}}^{q-\frac{1}{2}}\right)\right\}, \quad (2.20.a)$$

$$\sigma_{yy}{}^{q}_{m+\frac{1}{2},n} = \sigma_{yy}{}^{q-1}_{m+\frac{1}{2},n} + \frac{\partial t}{\partial x}\left\{\lambda\left(v^{q-\frac{1}{2}}_{x_{m,n}} - v^{q-\frac{1}{2}}_{x_{m-1,n}}\right) + (\lambda+2\mu)\left(v^{q-\frac{1}{2}}_{y_{m+\frac{1}{2},n+\frac{1}{2}}} - v^{q-\frac{1}{2}}_{y_{m+\frac{1}{2},n-\frac{1}{2}}}\right)\right\}, \quad (2.20.b)$$

$$\sigma_{xy}{}^{q}_{m,n+\frac{1}{2}} = \sigma_{xy}{}^{q-1}_{m,n+\frac{1}{2}} - \frac{\partial t}{\partial x}\,\mu\left(v^{q-\frac{1}{2}}_{y_{m+\frac{1}{2},n+\frac{1}{2}}} - v^{q-\frac{1}{2}}_{y_{m-\frac{1}{2},n+\frac{1}{2}}} + v^{q-\frac{1}{2}}_{x_{m,n}} - v^{q-\frac{1}{2}}_{x_{m,n-1}}\right). \quad (2.20.c)$$

From Figure 5, the FDTD equations for velocity shown in Equation 2.21 are also obtained.

$$v^{q+\frac{1}{2}}_{x_{m,n}} = v^{q-\frac{1}{2}}_{x_{m,n}} - \frac{1}{\rho}\frac{\partial t}{\partial x}\left(\sigma_{xx}{}^{q}_{m+\frac{1}{2},n} - \sigma_{xx}{}^{q}_{m-\frac{1}{2},n} + \sigma_{xy}{}^{q}_{m,n+\frac{1}{2}} - \sigma_{xy}{}^{q}_{m,n-\frac{1}{2}}\right), \quad (2.21.a)$$

$$v^{q+\frac{1}{2}}_{y_{m+\frac{1}{2},n+\frac{1}{2}}} = v^{q-\frac{1}{2}}_{y_{m+\frac{1}{2},n+\frac{1}{2}}} - \frac{1}{\rho}\frac{\partial t}{\partial x}\left(\sigma_{xy}{}^{q}_{m,n+\frac{1}{2}} - \sigma_{xy}{}^{q}_{m-1,n+\frac{1}{2}} + \sigma_{yy}{}^{q}_{m+\frac{1}{2},n+\frac{1}{2}} - \sigma_{yy}{}^{q}_{m+\frac{1}{2},n-\frac{1}{2}}\right). \quad (2.21.b)$$

2.3.2.3 *Three-dimensional elastic wave equation computation using FDTD in stress and velocity formulation*

For the three-dimensional case, the elementary grid cell shown in Figure 6 is used for the three-dimensional staggered spatial finite difference method. This way of arranging the variables in the grid cell was first proposed by Madariaga [31] to discretize the equations of electrodynamics.

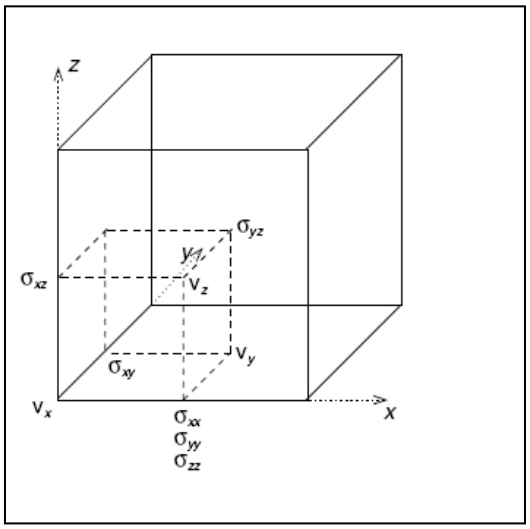

Figure 6 Three-dimensional FDTD grid cell for velocity and pressure in elastic solids

From the FDTD grid in Figure 6, FDTD equations for velocity and stress are obtained, as shown in Equation 2.22.

$$v_{x_{m,n,p}}^{q+\frac{1}{2}} = v_{x_{m,n,p}}^{q-\frac{1}{2}} - \frac{1}{\rho}\frac{\partial t}{\partial x}\left({\sigma_{xx}}_{m+\frac{1}{2},n,p}^{q} - {\sigma_{xx}}_{m-\frac{1}{2},n,p}^{q} + {\sigma_{xy}}_{m,n+\frac{1}{2},p}^{q} \right. \quad (2.22.a)$$

$$\left. - {\sigma_{xy}}_{m,n-\frac{1}{2},p}^{q} + {\sigma_{xz}}_{m,n,p+\frac{1}{2}}^{q} - {\sigma_{xz}}_{m,n,p-\frac{1}{2}}^{q} \right),$$

$$v_{y_{m+\frac{1}{2},n+\frac{1}{2},p}}^{q+\frac{1}{2}} = v_{y_{m+\frac{1}{2},n+\frac{1}{2},p}}^{q-\frac{1}{2}}$$
$$-\frac{1}{\rho}\frac{\partial t}{\partial x}\Big({\sigma_{xy}}_{m,n+\frac{1}{2},p}^{q} - {\sigma_{xy}}_{m-1,n+\frac{1}{2},p}^{q} + {\sigma_{yy}}_{m+\frac{1}{2},n,p}^{q}$$
$$- {\sigma_{yy}}_{m+\frac{1}{2},n-1,p}^{q} + {\sigma_{yz}}_{m+\frac{1}{2},n+\frac{1}{2},p+\frac{1}{2}}^{q}$$
$$- {\sigma_{yz}}_{m-1,n+\frac{1}{2},p-\frac{1}{2}}^{q}\Big), \qquad (2.22.b)$$

$$v_{z_{m+\frac{1}{2},n+\frac{1}{2},p+\frac{1}{2}}}^{q+\frac{1}{2}} = v_{z_{m+\frac{1}{2},n+\frac{1}{2},p+\frac{1}{2}}}^{q-\frac{1}{2}}$$
$$-\frac{1}{\rho}\frac{\partial t}{\partial x}\Big({\sigma_{xz}}_{m,n,p+\frac{1}{2}}^{q} - {\sigma_{xz}}_{m-1,n,p+\frac{1}{2}}^{q}$$
$$+ {\sigma_{yz}}_{m+\frac{1}{2},n+\frac{1}{2},p+\frac{1}{2}}^{q} - {\sigma_{yz}}_{m+\frac{1}{2},n-\frac{1}{2},p+\frac{1}{2}}^{q} + {\sigma_{zz}}_{m+\frac{1}{2},n,p}^{q}$$
$$- {\sigma_{zz}}_{m+\frac{1}{2},n,p-1}^{q}\Big), \qquad (2.22.c)$$

$${\sigma_{xx}}_{m+\frac{1}{2},n,p}^{q} = {\sigma_{xx}}_{m+\frac{1}{2},n,p}^{q-1}$$
$$+\frac{\partial t}{\partial x}\Big\{(\lambda+2\mu)\Big(v_{x_{m,n,p}}^{q-\frac{1}{2}} - v_{x_{m-1,n,p}}^{q-\frac{1}{2}}\Big)$$
$$+\lambda\Big(v_{y_{m+\frac{1}{2},n+\frac{1}{2},p}}^{q-\frac{1}{2}} - v_{y_{m+\frac{1}{2},n-\frac{1}{2},p}}^{q-\frac{1}{2}}\Big)$$
$$+\lambda\Big(v_{z_{m+\frac{1}{2},n,p+\frac{1}{2}}}^{q-\frac{1}{2}} - v_{z_{m+\frac{1}{2},n,p-\frac{1}{2}}}^{q-\frac{1}{2}}\Big)\Big\}, \qquad (2.22.d)$$

$$\sigma_{yy}{}^{q}_{m+\frac{1}{2},n,p} = \sigma_{yy}{}^{q-1}_{m+\frac{1}{2},n,p} + \frac{\partial t}{\partial x}\left\{\lambda\left(v^{q-\frac{1}{2}}_{x_{m,n,p}} - v^{q-\frac{1}{2}}_{x_{m-1,n,p}}\right) + (\lambda + 2\mu)\left(v^{q-\frac{1}{2}}_{y_{m+\frac{1}{2},n+\frac{1}{2},p}} - v^{q-\frac{1}{2}}_{y_{m+\frac{1}{2},n-\frac{1}{2},p}}\right) + \lambda\left(v^{q-\frac{1}{2}}_{z_{m+\frac{1}{2},n,p+\frac{1}{2}}} - v^{q-\frac{1}{2}}_{z_{m+\frac{1}{2},n,p-\frac{1}{2}}}\right)\right\}, \quad (2.22.e)$$

$$\sigma_{yy}{}^{q}_{m+\frac{1}{2},n,p} = \sigma_{yy}{}^{q-1}_{m+\frac{1}{2},n,p} + \frac{\partial t}{\partial x}\left\{\lambda\left(v^{q-\frac{1}{2}}_{x_{m,n,p}} - v^{q-\frac{1}{2}}_{x_{m-1,n,p}}\right) + \lambda\left(v^{q-\frac{1}{2}}_{y_{m+\frac{1}{2},n+\frac{1}{2},p}} - v^{q-\frac{1}{2}}_{y_{m+\frac{1}{2},n-\frac{1}{2},p}}\right) + (\lambda + 2\mu)\left(v^{q-\frac{1}{2}}_{z_{m+\frac{1}{2},n,p+\frac{1}{2}}} - v^{q-\frac{1}{2}}_{z_{m+\frac{1}{2},n,p-\frac{1}{2}}}\right)\right\}, \quad (2.22.f)$$

$$\sigma_{yz}{}^{q}_{m+\frac{1}{2},n+\frac{1}{2},p+\frac{1}{2}} = \sigma_{yz}{}^{q-1}_{m+\frac{1}{2},n+\frac{1}{2},p+\frac{1}{2}} - \frac{\partial t}{\partial x}\,\mu\left(v^{q-\frac{1}{2}}_{y_{m+\frac{1}{2},n+\frac{1}{2},p}} - v^{q-\frac{1}{2}}_{y_{m+\frac{1}{2},n+\frac{1}{2},p-1}} + v^{q-\frac{1}{2}}_{z_{m+\frac{1}{2},n,p+\frac{1}{2}}} - v^{q-\frac{1}{2}}_{z_{m+\frac{1}{2},n-1,p+\frac{1}{2}}}\right), \quad (2.22.g)$$

$$\sigma_{xz}{}^{q}_{m,n,p+\frac{1}{2}} = \sigma_{xz}{}^{q-1}_{m,n,p+\frac{1}{2}} - \frac{\partial t}{\partial x}\,\mu\left(v_{x_{m,n,p}}^{q-\frac{1}{2}} - v_{x_{m,n,p-1}}^{q-\frac{1}{2}} + v_{z_{m+\frac{1}{2},n,p+\frac{1}{2}}}^{q-\frac{1}{2}} - v_{z_{m-\frac{1}{2},n,p+\frac{1}{2}}}^{q-\frac{1}{2}} \right), \tag{2.22.h}$$

$$\sigma_{xy}{}^{q}_{m,n+\frac{1}{2},p} = \sigma_{xy}{}^{q-1}_{m,n+\frac{1}{2},p} - \frac{\partial t}{\partial x}\,\mu\left(v_{y_{m+\frac{1}{2},n+\frac{1}{2},p}}^{q-\frac{1}{2}} - v_{y_{m-\frac{1}{2},n+\frac{1}{2},p}}^{q-\frac{1}{2}} + v_{x_{m,n,p}}^{q-\frac{1}{2}} - v_{x_{m,n-1,p}}^{q-\frac{1}{2}} \right). \tag{2.22.i}$$

2.3.3 Poroelastic Wave Equation Computation Using FDTD without Boundary Layers in Stress and Velocity Formulation

2.3.3.1 *One-dimensional poroelastic wave equation computation using FDTD in stress and velocity formulation*

The grid for this case is shown in Figure 7. It is similar to the grid for elastic waves. The variables v^s and v^f are both represented by V at the center of the cell. P_f and σ are both represented by S, offset by half in time and space of the cell [6].

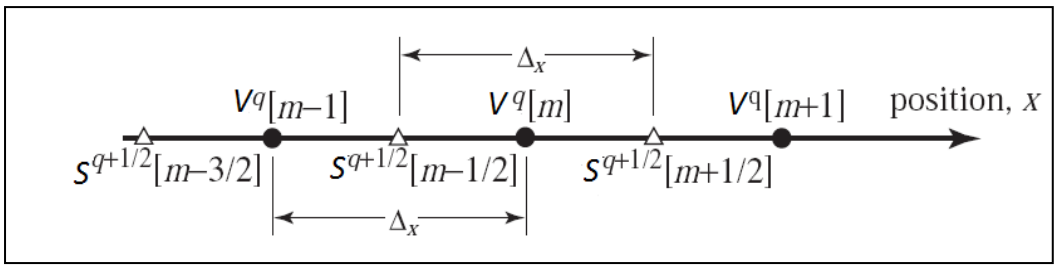

Figure 7 One-dimensional FDTD grid for poroelastic solid

For the one-dimensional case, FDTD equations for stress and velocity are obtained, as shown in Equation 2.23.

$$v_{x\,m}^{s\,q} = v_{x\,m}^{s\,q-1} + \frac{\rho_w}{\rho_w\rho - \rho_f^2}\frac{\partial t}{\partial x}\left(\sigma_{xx}^{\;\;q+\frac{1}{2}}{}_{m+\frac{1}{2}} - \sigma_{xx}^{\;\;q+\frac{1}{2}}{}_{m-\frac{1}{2}} \right) + \rho_f \left(P^{f\;\;q+\frac{1}{2}}_{m+\frac{1}{2}} - P^{f\;\;q+\frac{1}{2}}_{m-\frac{1}{2}} \right) + \rho K\, v_{x\,m}^{f}\,, \tag{2.23.a}$$

$$v_{x\,m}^{f\,q} = v_{x\,m}^{f\,q-1} - \frac{\rho_f}{\rho_w\rho - \rho_f^2}\frac{\partial t}{\partial x}\left(\sigma_{xx}^{\;\;q+\frac{1}{2}}{}_{m+\frac{1}{2}} - \sigma_{xx}^{\;\;q+\frac{1}{2}}{}_{m-\frac{1}{2}} \right) - \rho \left(P^{f\;\;q+\frac{1}{2}}_{m+\frac{1}{2}} - P^{f\;\;q+\frac{1}{2}}_{m-\frac{1}{2}} \right) - \rho_f K\, v_{x\,m}^{f}\,, \tag{2.23.b}$$

$$\sigma_x^{\;\;q+\frac{1}{2}}{}_{m+\frac{1}{2}} = \sigma_x^{\;\;q-\frac{1}{2}}{}_{m+\frac{1}{2}} + \partial t \left\{ \frac{\lambda_s + 2\,\mu}{\partial x}\left(v_{x\,m,n}^{s\,q} - v_{x\,m-1,n}^{s\,q} \right) + \lambda_s \left(v_y^{s\;\;q+\frac{1}{2}}{}_{m+\frac{1}{2}} - v_y^{s\;\;q+\frac{1}{2}}{}_{m+\frac{1}{2}} \right) - \alpha \left(P^{f\;\;q+\frac{1}{2}}_{m+\frac{1}{2}} - P^{f\;\;q-\frac{1}{2}}_{m+\frac{1}{2}} \right) \right\}, \tag{2.23.c}$$

$$P^{f\;\;q+\frac{1}{2}}_{m+\frac{1}{2}} = P^{f\;\;q-\frac{1}{2}}_{m+\frac{1}{2}} - \alpha M \left(v_{x\,m}^{s} - v_{x\,m-1}^{s} \right) - M \left(v_{x\,m}^{f} - v_{x\,m-1}^{f} \right). \tag{2.23.d}$$

2.3.3.2 *Two-dimensional poroelastic wave equation computation using FDTD in stress and velocity formulation*

There are various approaches to creating a grid for the four variables of the wave of this type. Additional variables can be introduced to the FDTD equations of this model to make the computation easier. The FDTD equations of this model without the addition of any extra variables are presented in Figure 8.

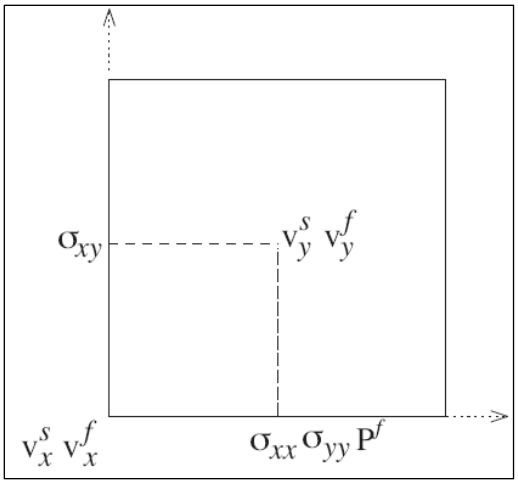

Figure 8 Two-dimensional FDTD grid cell for poroelastic solids

The cell in Figure 8 can be used to discretize the poroelastic two-dimensional equation to the FDTD form with v_x^s and v_x^f at the center of the grid and other parameters offset in space or time relative to velocity.

The FDTD equations obtained for the two-dimensional case from Figure 8 are shown in Equation 2.24.

$$
\begin{aligned}
v_{x\,m,n}^{s\,q} = v_{x\,m,n}^{s\,q-1} &\\
&+ \frac{\rho_w}{\rho_w\rho - \rho_f^2}\frac{\partial t}{\partial x}\left(\sigma_{xx}^{\,q+\frac{1}{2}}{}_{m+\frac{1}{2},n} - \sigma_{xx}^{\,q+\frac{1}{2}}{}_{m-\frac{1}{2},n} \right. \\
&\left. + \sigma_{xy}^{\,q+\frac{1}{2}}{}_{m,n+\frac{1}{2}} - \sigma_{xy}^{\,q+\frac{1}{2}}{}_{m,n-\frac{1}{2}} \right) \\
&+ \rho_f \left(P^f{}_{m+\frac{1}{2},n}^{\;\;q+\frac{1}{2}} - P^f{}_{m-\frac{1}{2},n}^{\;\;q+\frac{1}{2}} \right) + \rho K\, v_{x\,m,n}^f,
\end{aligned}
\qquad (2.24.a)
$$

$$
\begin{aligned}
v_y^{s\,q}{}_{m,n} = v_y^{s\,q-1}{}_{m,n} & \\
& + \frac{\rho_w}{\rho_w\rho - \rho_f^2}\frac{\partial t}{\partial x}\left(\sigma_{xx}^{\,q+\frac{1}{2}}{}_{m+\frac{1}{2},n} - \sigma_{xx}^{\,q+\frac{1}{2}}{}_{m-\frac{1}{2},n} \right. \\
& \left. + \sigma_{xy}^{\,q+\frac{1}{2}}{}_{m,n+\frac{1}{2}} - \sigma_{xy}^{\,q+\frac{1}{2}}{}_{m,n-\frac{1}{2}} \right) \\
& + \rho_f \left(P^f{}_{m+\frac{1}{2},n}^{\;\;q+\frac{1}{2}} - P^f{}_{m-\frac{1}{2},n}^{\;\;q+\frac{1}{2}} \right) + \rho K\, v_y^f{}_{m,n},
\end{aligned}
\tag{2.24.b}
$$

$$
\begin{aligned}
v_x^{f\,q}{}_m = v_x^{f\,q-1}{}_m - \frac{\rho_f}{\rho_w\rho - \rho_f^2}\frac{\partial t}{\partial x}\left(\sigma_{xx}^{\,q+\frac{1}{2}}{}_{m+\frac{1}{2}} - \sigma_{xx}^{\,q+\frac{1}{2}}{}_{m-\frac{1}{2}} \right. & \\
\left. + \sigma_{xx}^{\,q+\frac{1}{2}}{}_{m+\frac{1}{2}} - \sigma_{xx}^{\,q+\frac{1}{2}}{}_{m-\frac{1}{2}} \right) - \rho\left(P^f{}_{m+\frac{1}{2}}^{\;\;q+\frac{1}{2}} - P^f{}_{m-\frac{1}{2}}^{\;\;q+\frac{1}{2}} \right) & \\
- \rho_f K\, v_x^f{}_m , &
\end{aligned}
\tag{2.24.c}
$$

$$
\begin{aligned}
v_y^{f\,q}{}_m = v_y^{f\,q-1}{}_m - \frac{\rho_f}{\rho_w\rho - \rho_f^2}\frac{\partial t}{\partial x}\left(\sigma_{xx}^{\,q+\frac{1}{2}}{}_{m+\frac{1}{2}} - \sigma_{xx}^{\,q+\frac{1}{2}}{}_{m-\frac{1}{2}} \right. & \\
\left. + \sigma_{xx}^{\,q+\frac{1}{2}}{}_{m+\frac{1}{2}} - \sigma_{xx}^{\,q+\frac{1}{2}}{}_{m-\frac{1}{2}} \right) - \rho\left(P^f{}_{m+\frac{1}{2}}^{\;\;q+\frac{1}{2}} - P^f{}_{m-\frac{1}{2}}^{\;\;q+\frac{1}{2}} \right) & \\
- \rho_f K\, v_y^f{}_m , &
\end{aligned}
\tag{2.24.d}
$$

$$
\begin{aligned}
\sigma_{xx}^{\,q+\frac{1}{2}}{}_{m+\frac{1}{2}} = \sigma_{xx}^{\,q-\frac{1}{2}}{}_{m+\frac{1}{2}} & \\
& + \partial t \left\{ \frac{\lambda_s + 2\,\mu}{\partial x}\left(v_x^{s\,q}{}_{m,n} - v_x^{s\,q}{}_{m-1,n} \right) \right. \\
& + \lambda_s \left(v_y^{s\,q+\frac{1}{2}}{}_{m+\frac{1}{2}} - v_y^{s\,q+\frac{1}{2}}{}_{m+\frac{1}{2}} \right) \\
& \left. - \alpha \left(P^f{}_{m+\frac{1}{2}}^{\;\;q+\frac{1}{2}} - P^f{}_{m+\frac{1}{2}}^{\;\;q-\frac{1}{2}} \right) \right\} ,
\end{aligned}
\tag{2.24.e}
$$

$$\sigma_{yy}{}^{q+\frac{1}{2}}_{m+\frac{1}{2}} = \sigma_{yy}{}^{q-\frac{1}{2}}_{m+\frac{1}{2}} + \partial t \left\{ \frac{\lambda_s + 2\,\mu}{\partial x} \left(v_x{}^{sq}_{m,n} - v_x{}^{sq}_{m-1,n} \right) + \lambda_s \left(v_y{}^{s\,q+\frac{1}{2}}_{m+\frac{1}{2}} - v_y{}^{s\,q+\frac{1}{2}}_{m+\frac{1}{2}} \right) \right\} - \alpha \left(P^f{}^{\,q+\frac{1}{2}}_{m+\frac{1}{2}} - P^f{}^{\,q-\frac{1}{2}}_{m+\frac{1}{2}} \right) \partial t \,, \tag{2.24.f}$$

$$\sigma_{xy}{}^{q+\frac{1}{2}}_{m+\frac{1}{2}} = \sigma_{xy}{}^{q-\frac{1}{2}}_{m+\frac{1}{2}} + \partial t \left\{ \frac{\lambda_s + 2\,\mu}{\partial x} \left(v_x{}^{sq}_{m,n} - v_x{}^{sq}_{m-1,n} \right) + \lambda_s \left(v_y{}^{s\,q+\frac{1}{2}}_{m+\frac{1}{2}} - v_y{}^{s\,q+\frac{1}{2}}_{m+\frac{1}{2}} \right) \right\} - \alpha \left(P^f{}^{\,q+\frac{1}{2}}_{m+\frac{1}{2}} - P^f{}^{\,q-\frac{1}{2}}_{m+\frac{1}{2}} \right) \partial t \,, \tag{2.24.g}$$

$$P^f{}^{\,q+\frac{1}{2}}_{m+\frac{1}{2}} = P^f{}^{\,q-\frac{1}{2}}_{m+\frac{1}{2}} - \alpha M \left(v_x{}^s_m - v_x{}^s_{m-1} + v_x{}^s_m - v_x{}^s_{m-1} \right) - M \left(v_x{}^f_m - v_x{}^f_{m-1} + v_x{}^f_m - v_x{}^f_{m-1} \right) \tag{2.24.h}$$

2.4 FDTD with Convolutional Perfectly Matched Layer (CPML)

The boundary regions in the FDTD simulations have to be terminated such that it will not result in a large amount of reflection of the waves from the boundary regions. The boundary conditions are made to be absorbing so that the ratio of reflected waves is less. These are thus called Absorbing Boundary Conditions (ABC). There are three grid truncation techniques for open-region FDTD that are most used [13]. They are the

Mur ABC, the Liao ABC, and various perfectly matched layer (PML) formulations. The advantage of the Mur ABC and Liao ABC techniques are that they are simpler than PML techniques [22]. The advantage of the PML technique is that it can provide orders-of-magnitude lower reflections [23].

The classical method of implementing PML is called Berenger's classical split field implementation of PML, which was discovered by Berenger [24][27] in 1994. He improved on the existing FDTD by introducing a technique that would create a perfectly matched layer between the boundary of the FDTD and the edge of the grid [25]. However, perfectly matched layers resulted in reflection from the boundary layer that took a longer time to die down [26]. Since then, the classical split PML has been modified and extended to the Uniaxial PML (UPML), the Convolutional PML (CPML), and the higher-order PML.

The importance of the CPML [14] and UPML [9] implementations of FDTD over the classical PML implementation of FDTD is that they have increased the ability to absorb evanescent waves [15]. So the material to be simulated can be placed closer to a simulated scattering or radiating structure than in Berenger's classical split PML implementation of FDTD [16]. Also, the memory requirement for CPML is less compared to Berenger's PML [19].

The boundary condition that will be used in this project is the CPML. Though CPML techniques look superior to classical PML techniques, they take a longer computation time [5].

CHAPTER 3

METHODS AND RESULTS

The two-dimensional CPML FDTD was tested for poroelastic solids using Matlab. This was done in the velocity and stress formulation and not in the displacement and stress formulation.

3.1 Program 1. The Wave Propagation in Two-dimensional Poroelastic Media

3.1.1 Geometry

A homogenous medium of size 100 mm by 100 mm was used. It was surrounded by four CPML layers of 10 grid points each. The size of the grid cell was assumed to be 1mm by 1mm. The time duration of the simulation was run for 400 ms with the smallest time duration being 0.1 μs.

The geometry of the poroelastic solid was assumed to be circular with one poroelastic solid inside the circle and another poroelastic material outside the circle. The radius of the circle was taken to be 20 mm as shown in Figure 9.

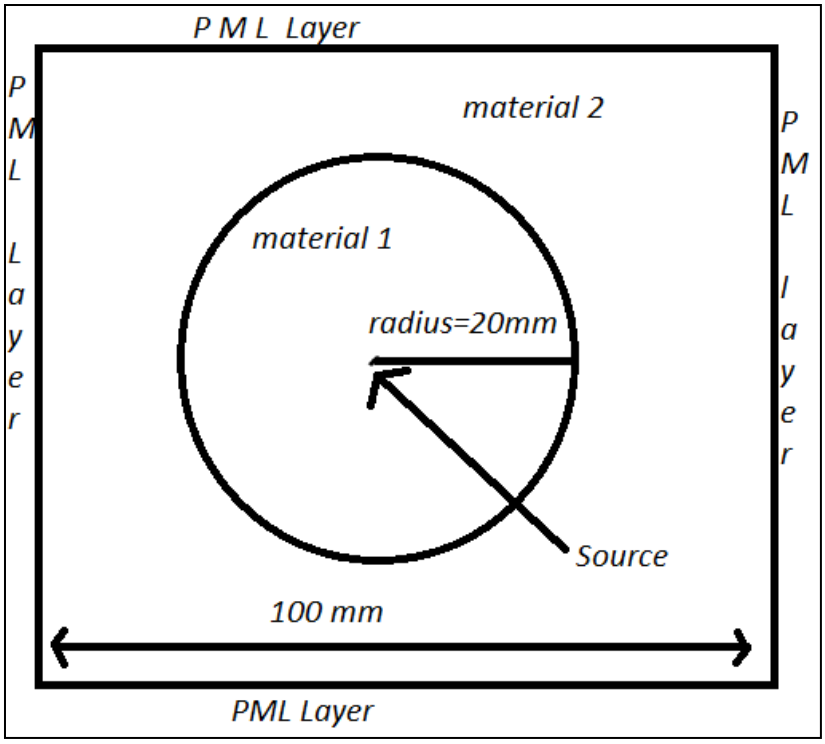

Figure 9 Geometry of the two-dimensional poroelastic solid

3.1.2 Parameters

The poroelastic material inside the circle was assumed to be mud saturated with water. The poroelastic material outside the circle was assumed to be mud that was slightly more porous than the material inside the circle. The parameters for the two materials used in the simulation are shown in Table 4.

Table 4 Fluid and Solid parameters used in the simulation [6]

Physical variables	Units (IS)	Lower layer	Upper layer
Solid density ρ_s	kg/m^3	2588	2250
Fluid density ρ_f	kg/m^3	952.4	1040
Matrix tortuosity a		2.49	2.42
Porosity ϕ		0.25	0.1
Bulk density $\rho = \varphi\rho_f + (1 - \varphi)\rho_s$	kg/m^3	2179.1	2129
Apparent density $\rho_w = a\rho_f/\varphi$	kg/m^3	9486	25168
α		0.89	0.58
M	Pa	7.71×10^9	7.34×10^9
Damping viscous term K	Ns/m^4	3.38×10^5	3.33×10^6
Fast pressure-wave velocity in the solid V_{Pf}	m/s	2817.33	1921
Slow pressure-wave velocity in the solid V_{Ps}	m/s	740	452.73
Shear-wave velocity in the solid V_S	m/s	1587.4	1072.6
Shear modulus μ	m/s	5.25×10^9	2.4×10^9
Lamé coefficient in solid matrix λ_s	Pa	6.2×10^8	6.0×10^8
Lamé coefficient in saturated medium $\lambda = \lambda_s + M\alpha^2$	Pa	6.7271×10^9	3.069×10^9

3.1.3 Courant Number

Using the *dt* and *dx* values, the Courant number was calculated with the same method used to calculate the Courant number in the elastic wave equations [6]. It was taken care that the value of the Courant number was not above 1 or else the simulation

would turn out to be unstable. Substituting the values of *dx*, *dy*, *dt*, and c_p with, respectively, 1921000 mm/s, 10^{-7} s, 1 mm, and 1 mm, we obtain a Courant number of 0.2, which is well within the stability criterion of 1.

3.1.4 Source Location, Type, and Values

The source was located in the middle of the circle. Its location can be changed very easily anywhere in the geometry. Three types of sources were used in the simulation. They were a Gaussian source, the first derivative of a Gaussian source, and the second derivative of a Gaussian source.

The equations used for the three source types are shown in Equation 3.1.

$$G = factor * e^{-a(t-t_0)^2}, \quad (3.1.a)$$

$$FDG = factor * 2 * a * (t - t_0) * e^{-a(t-t_0)^2}, \quad (3.1.b)$$

$$SDG = factor * (1 - 2a(t - t_0)^2) * e^{-a(t-t_0)^2}. \quad (3.1.c)$$

In Equation 3.1, the terms *G*, *FDG*, *SDG*, *factor*, *a*, and t_0 represent, respectively, the Gaussian source, the first derivative of the Gaussian source, the second derivative of the Gaussian source, the amplification factor of the source, an arbitrary constant used to influence the time variable, and the time of origin of the source. The increasing derivatives of the Gaussian source showed differences with time because of the introduction of the $(t-t_0)$ term in the first derivative and the $(t-t_0)^2$ terms in the second derivative.

The frequency of the source was taken to be 80 KHz. The amplification factor of the source was taken to be 100. It was time shifted for better clarity of the output graphs. It is to be noted that the frequency of the source and the velocity of the poroelastic solid

should give a wavelength which is less than the size of the discrete cell, which is 1mm. The angle of the source force could also be varied. An angle source of 0 degrees was used in this case.

Here, we have that the wavelength of the wave is equal to the ratio of the velocity of the wave to the frequency of the source. So the result is a wavelength of 0.5 mm, which is smaller than the size of the cell which is 1 mm. Thus using the values of the sources, the source force along the *x* and *y* directions were computed as shown below:

$$Force_x = \sin(angle) * source\ , \tag{3.2.a}$$

$$Force_y = \cos(angle) * source. \tag{3.2.b}$$

In the above equations, the variables named $Force_x$ and $Force_y$ represent the force of impact of the source. The constant named *angle* represents the angle of the source. The term named *source* may represent any of the three types of sources mentioned before. The forces were then used to create the disturbance in the material by adding it to the velocity terms (v_x and v_y) of the material with density ρ, as shown in Equation 3.3.

$$v_x = v_x + \frac{(Force_x * dt)}{\rho}, \tag{3.3.a}$$

$$v_y = v_y + \frac{\left(Force_y * dt\right)}{\rho}. \tag{3.3.b}$$

3.1.5 CPML Values

The CPML layers were implemented on all four sides of the grid. The equations used to calculate the values of *d* and α were taken from Rodney and Gedney [8].

For the CPML in the *x* direction, the equations used are shown in Equation 3.4.

$$d_0 = -(N+1)\frac{C_p \log(rcoef)}{2\,L_{xpml}}, \tag{3.4.a}$$

$$d_x(x) = d_0\left(\frac{x}{L_{xpml}}\right)^N, \tag{3.4.b}$$

$$\alpha_x = \alpha_{max}\left(1 - \frac{x}{L_{xpml}}\right), \tag{3.4.c}$$

$$\alpha_{max} = \pi\, f_{source}, \tag{3.4.d}$$

$$K_x = 1 + (k_{max} - 1)\, x^N, \tag{3.4.e}$$

$$b = e^{-\left(\frac{d_x}{k_x} + \alpha_x\right)} * dt, \tag{3.4.f}$$

$$a = \frac{d_x(b_x - 1)}{k_x(d_x + k_x\,\alpha_x)}. \tag{3.4.g}$$

The variables d_x, α_x, and k_x represent, respectively, damping factor, angular frequency, and amplification in the *x* direction. The variables *a* and *b* are terms used to modify temporary memory variables of stress. The constants d_0, α_{max}, L_{xpml}, f_{source}, k_{max}, *rcoef*, *N*, and C_p represent, respectively, maximum damping constant, maximum frequency of the source, length of the PML, frequency of the source, maximum reflection co-efficient, number of points in the grid, and velocity of the wave. Similar values were used for the *y* direction.

For the CPML in the *y* direction, the equations used are shown in Equation 3.5.

$$d_0 = -(N+1)\frac{C_p \log(rcoef)}{2\,L_{ypml}}, \tag{3.5.a}$$

$$d_y(y) = d_0\left(\frac{y}{L_{ypml}}\right)^N, \tag{3.5.b}$$

$$\alpha_y = \alpha_{max}\left(1 - \frac{y}{L_{ypml}}\right), \tag{3.5.c}$$

$$\alpha_{max} = \pi\, f_{source}\,, \tag{3.5.d}$$

$$K_y = 1 + (k_{max} - 1)\, y^N\,, \tag{3.5.e}$$

$$b = e^{-\left(\frac{d_y}{k_y} + \alpha_y\right)} * dt\,, \tag{3.5.f}$$

$$a = \frac{d_y(b_y - 1)}{k_y(d_y + k_y\,\alpha_y)}. \tag{3.5.g}$$

These values were used to calculate a value for the temporary memory variable for stress, velocity, and pressure. The temporary memory variable used is shown in Equation 3.6.

$$\psi_x = b_x\,\psi_x^{n-1} + a_x\left(\frac{\partial}{\partial x}\right)^{n-1}. \tag{3.6}$$

The temporary memory variable in the *x* direction shown here was added to each of the values of velocity, pressure, and stress. For a one-dimensional case, one such computation of velocity is shown in Equation 3.7.

$$\frac{\partial v_x}{\partial t} = -\frac{1}{\rho}\left(\frac{1}{k_x}\frac{\partial}{\partial x} + \psi_x\right)\sigma_x\,. \tag{3.7}$$

These same values were then repeated for the *y* direction as well. The graphs for the values of *d*, *α*, *a*, and *b* in the *x* direction are shown in Figures 10, Figure 11, Figure 12, and Figure 13. Similar graphs can be obtained for the *y* direction.

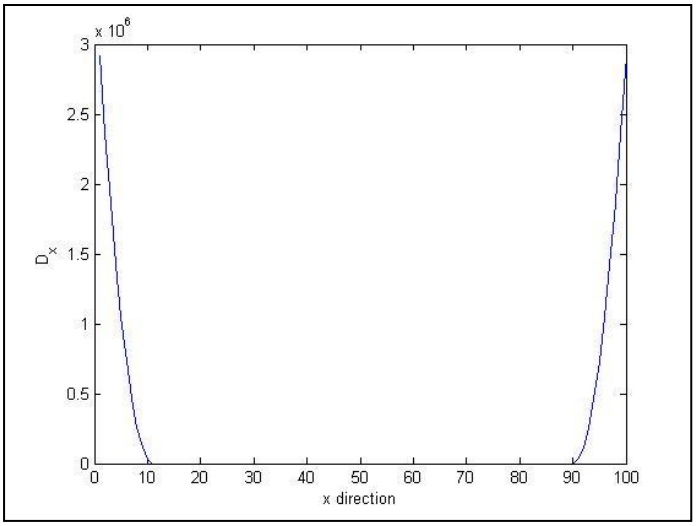

Figure 10 Damping profile of a CPML parameter

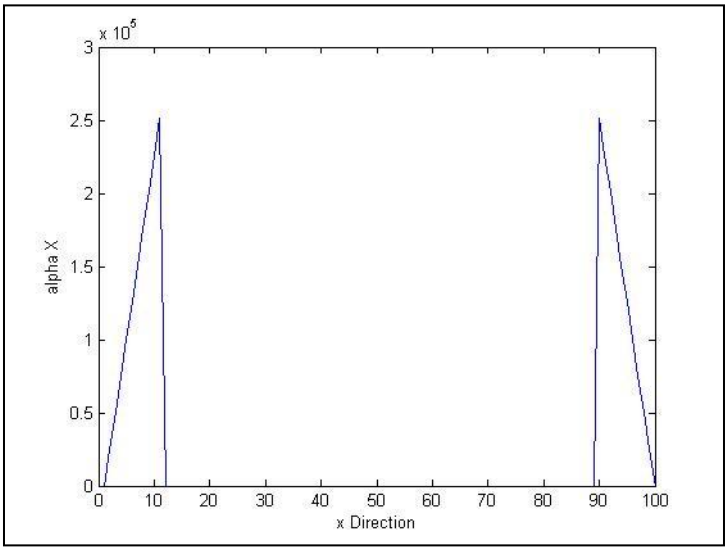

Figure 11 Profile of CPML parameter α

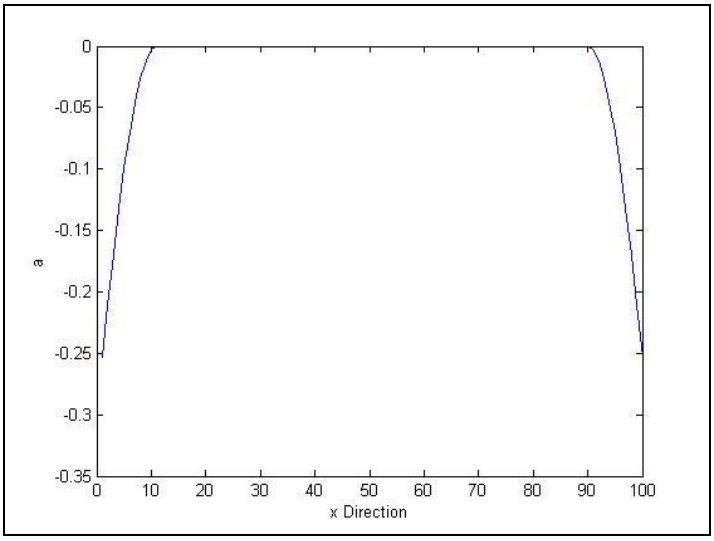

Figure 12 Profile of CPML parameter *a*

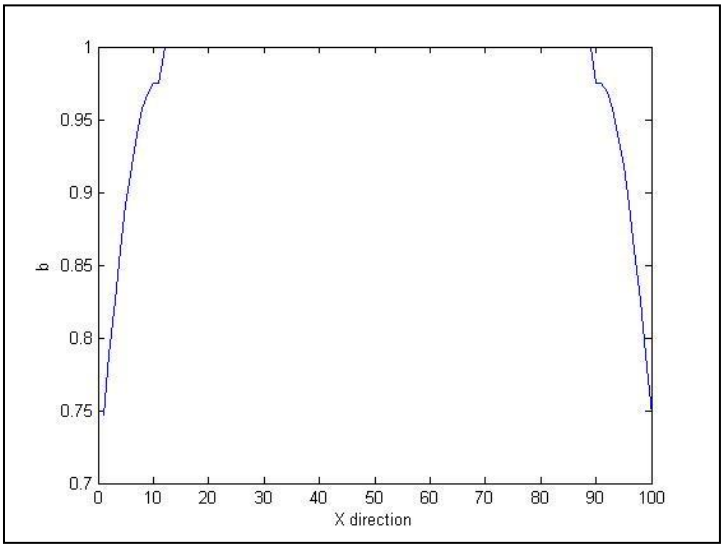

Figure 13 Profile of CPML parameter *b*

It is observed that the CPML has a width of 10 at each side. Thus, damping is seen only in the CPML region. It is also to be observed that the value of *K* is taken to be constant in this program, thus making it easier for the FDTD calculations.

3.1.6 Type of FDTD Used and Dirichlet's Condition

A staggered spatial finite difference grid was used. It is a leapfrog technique popularized by Allen Taflove [2] and first introduced by Yee [1].

On the external edges of the grid, i.e., at the top of each PML, a Dirichlet's condition was imposed on the velocity vector for the whole duration of the simulation. This gives v equals to zero for all t.

3.1.7 Image Plots

All the variables were plotted against time by using an *imagesc()* function in Matlab, which gives a two-dimensional image plot of the variable. Using the *frame=getframe()* function, a movie was made out of a series of two-dimensional plots.

3.1.8 Receivers

The receivers that output the graph of the velocity and pressure were taken to be on the top of the source and at the edge of the circle. So, there were two receivers in the geometry. Their locations were (50 mm, 50 mm) and (25mm, 50mm). Each of them could be placed at any desirable position, but the given two locations were chosen for their ease of visualization. The values recorded from the receivers were velocity of the solid, velocity of the fluid, pressure, and stress in the solid. Two sets of graphs were obtained for each of these 4 variables, one in the x direction and another in the y direction.

3.1.9 Results Obtained When the Source is a Gaussian Pulse

A graph of the various variables was obtained with respect to time at the two receiver locations with a different source type. It was observed here that the time difference between the largest amplitude wave in the source and the largest amplitude

wave in the edge occurs because of the time taken for the wave to travel from the source to the edge of the cell. A graph of fluid pressure in the material is shown in Figure 14.

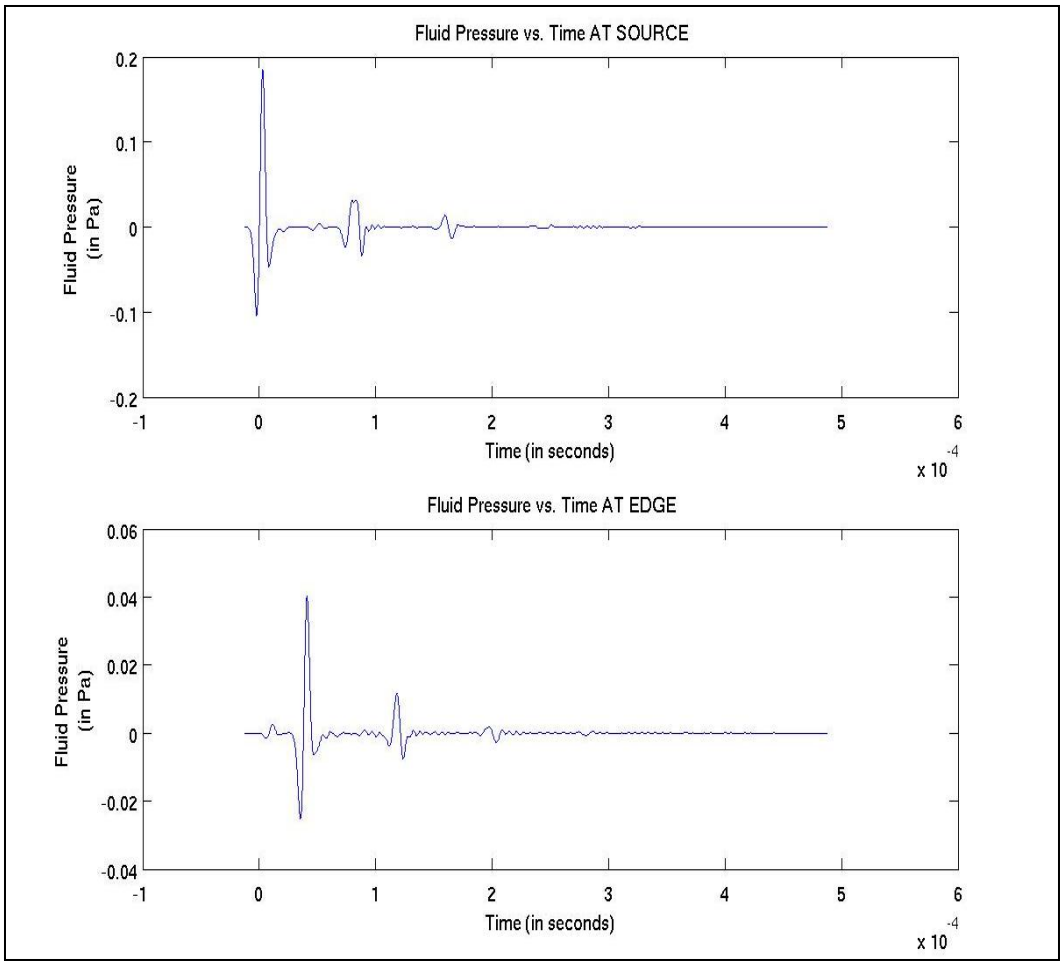

Figure 14 Fluid pressure for source type Gaussian

The stress components in the solid part of the material undergo compression and shear. A large number of oscillations are seen in the *xy* axis rather than in the *xx* or *yy* axis. This was because of the alignment of the angle force, which was taken to be 45 degree with respect to the *x* axis.

The fluid in the porous material cannot undergo shear. In fact, fluids have zero shear modulus. Only compression waves are seen in the fluid. But in the poroelastic case, the compression wave is a combination of the compressions of the solid and the fluid.

A graph of solid stress in the material is shown in Figure 15. The solid part of a porous material can undergo compression and shear; thus there are two wave velocities seen in the waveform in Figure 15: the fast P wave and the slow P wave along the *x* direction and the shear wave S along the *y* direction. From Figure 15, the velocity of the fast and slow wave was also obtained.

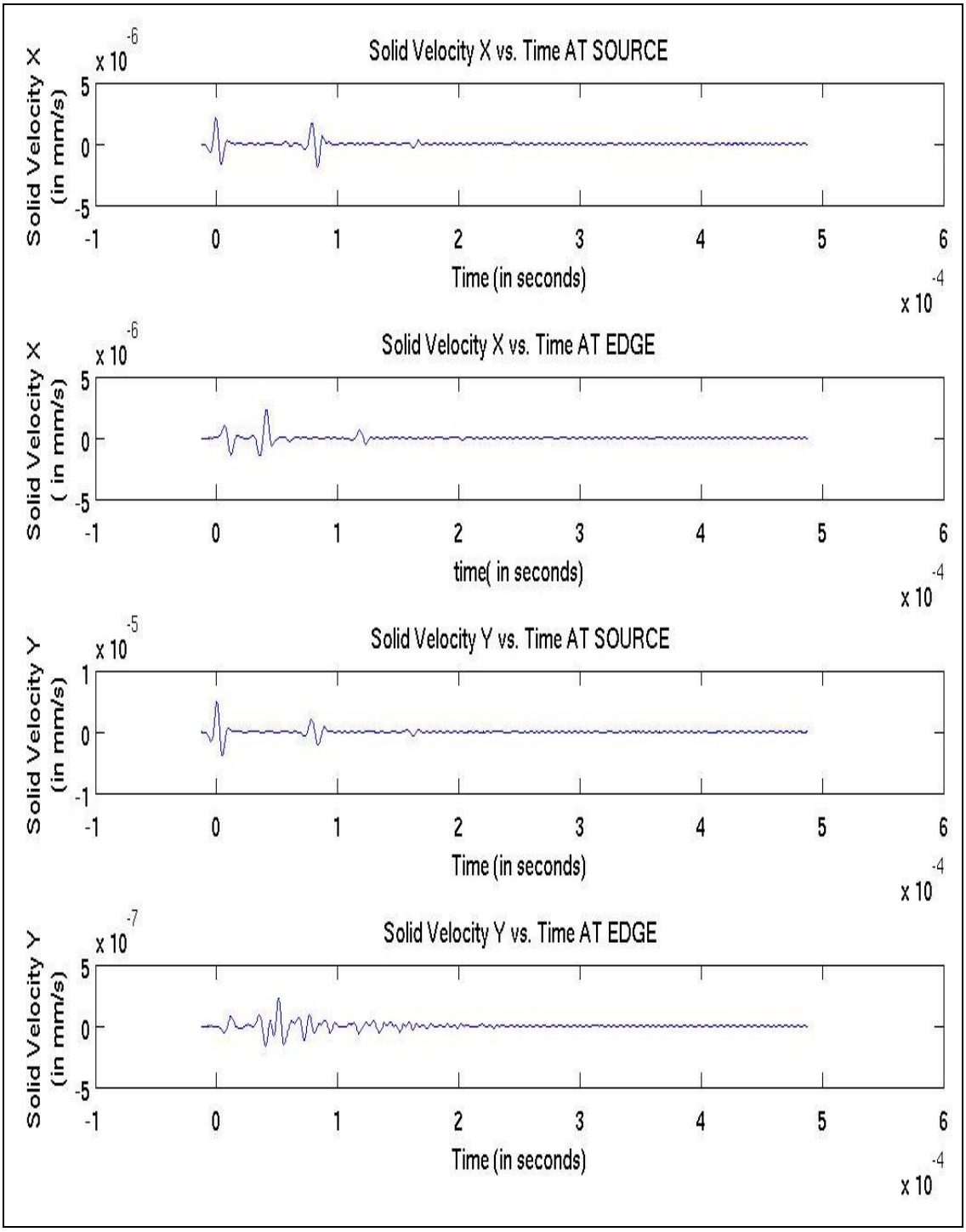

Figure 15 Solid velocity for source type Gaussian

3.1.10 Results Obtained When the Source is a First Derivative of a Gaussian Pulse

For the first derivative of a Gaussian as a source, the t-t_0 term introduces numerous oscillations, as shown in Figure 16.

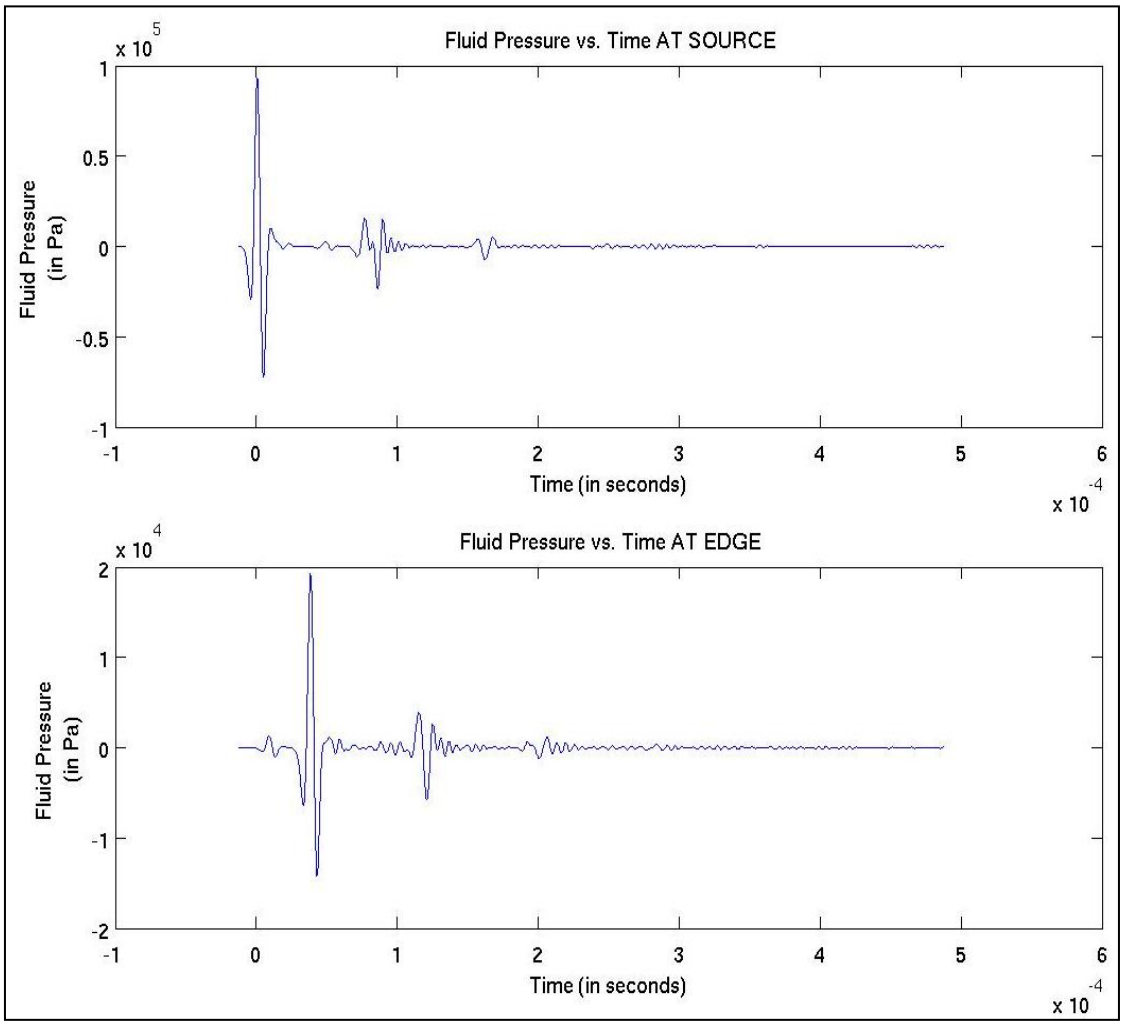

Figure 16 Fluid Pressure for source type first derivative of Gaussian

If the graph for the receiver at the edge in Figure 16 is analyzed closely, a wave of small amplitude is seen before a higher amplitude wave arrives. The initial wave is the fast P wave. Since the fluid in the porous medium is assumed to be viscous, the fluid is

assumed to stick more readily to the sides of the pores; thus causing more disturbances to be transferred to the fluid. The solid velocity at the source and the edges are shown in Figure 17.

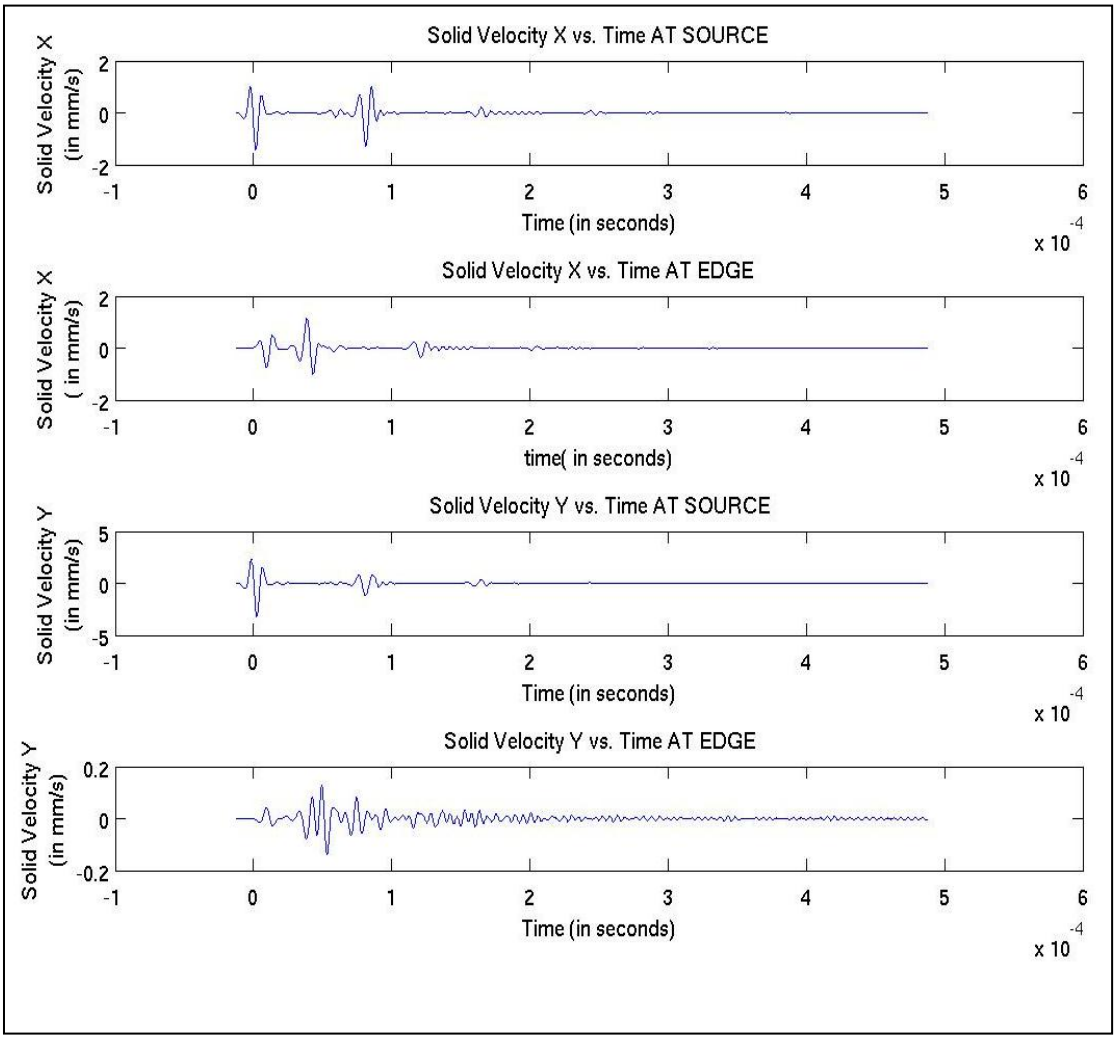

Figure 17 Solid velocity for source type of first derivative of Gaussian

3.1.11 Results Obtained When the Source is a Second Derivative of a Gaussian Pulse

The results obtained for the fluid pressure and solid velocity are shown in Figure 18 and Figure 19. The main difference between the graphs in Figure 16 from those in Figure 18 is the presence of two positive spikes due to the nature of the source.

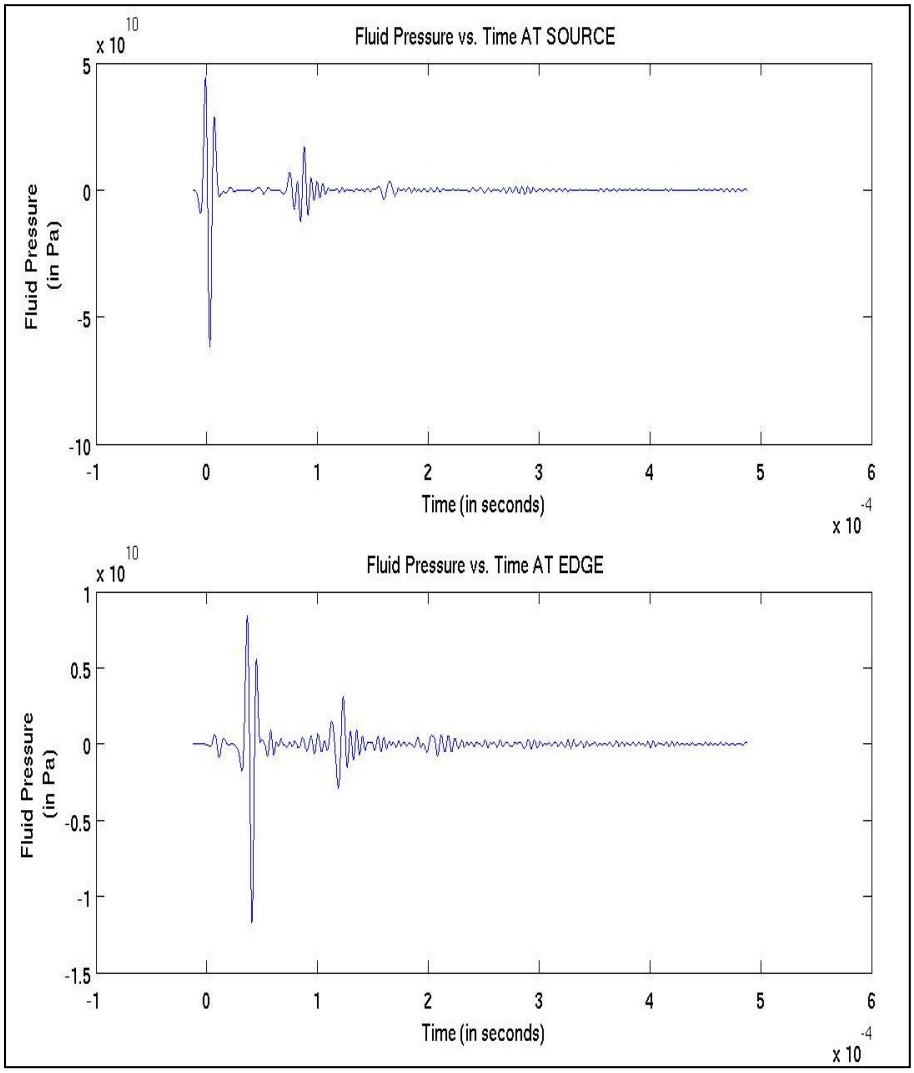

Figure 18 Fluid pressure for source type of second derivative of Gaussian

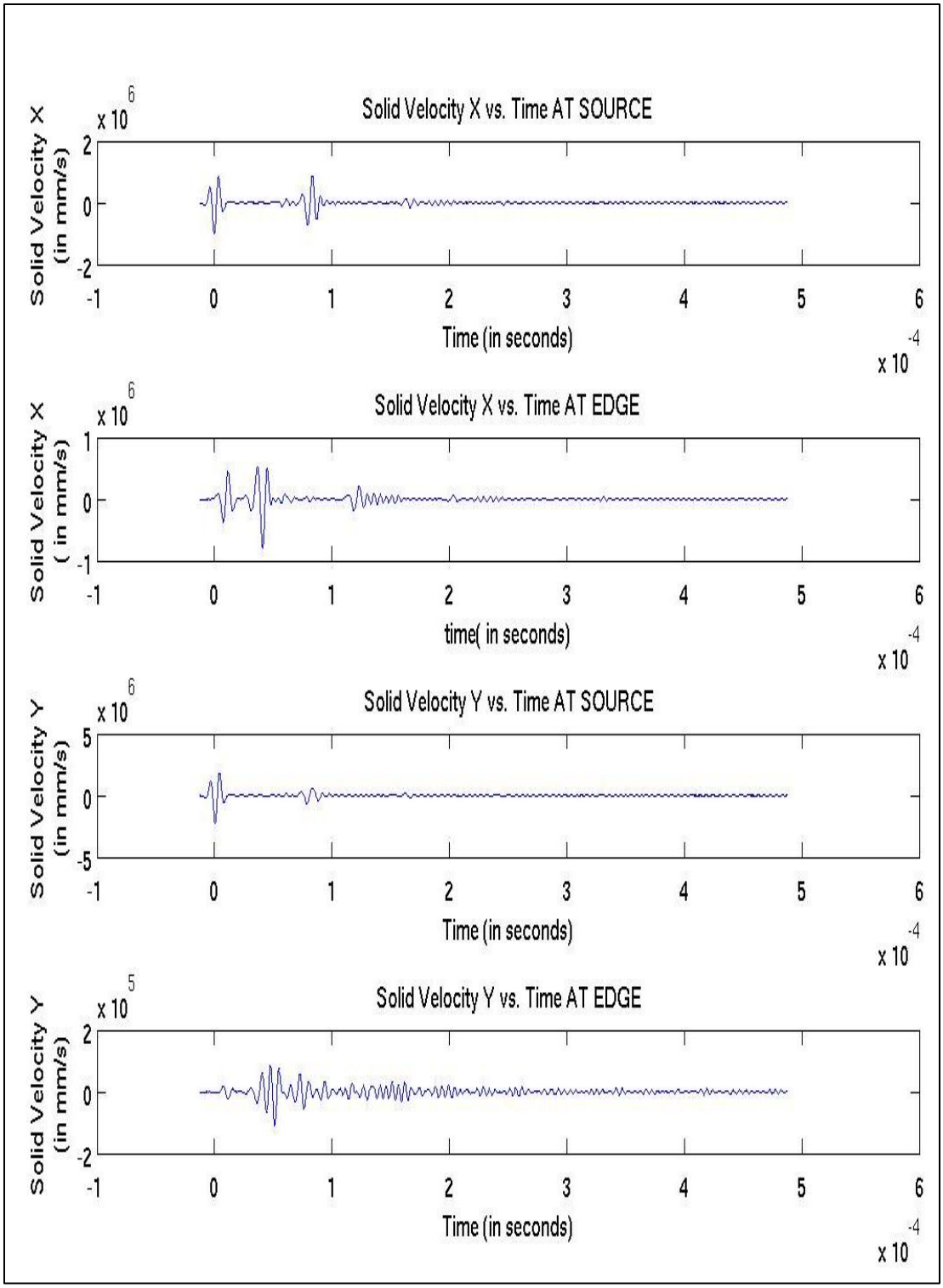

Figure 19 Solid velocity for source type of second derivative of Gaussian

3.1.12 Analysis of the Slow and Fast P Waves in Poroelastic Solid

The fast P wave velocity was calculated by dividing the distance travelled by the first wave from the source to the edge of the material by the time it takes for the first wave to hit the edge of the poroelastic material. This value was obtained to be 1886.2 m/s.

The slow P wave velocity was calculated by dividing the distance travelled by the second slower wave from the source to the edge of the material by the time it takes for the first wave to hit the edge of the poroelastic material. This value was obtained to be 413.22 m/s.

The theoretical values of the fast and slow P waves in the computation were taken to be 1921 m/sec and 452.73 m/s. Comparing the results obtained with these values, the accuracy of 1.8% was obtained for the fast P wave and an accuracy of 8.6% was obtained for the slow P wave. These errors could be attributed to the grid size considered and also the limitation of the source frequency considered.

3.2 Program 2. Wave Propagation in Two-dimensional Elastic Media

3.2.1 Geometry

A homogenous medium of size 100mm by 100 mm was used, surrounded by four CPML layers of 10 grid points each. The size of the grid cell was assumed to be 1mm by 1mm. The total iterations conducted were 20,000 with each iteration being $2*10^{-8}$ seconds long. This made the total duration of the simulation 400 ms, with the smallest time duration being 0.2 μs. The total number of grid points used in this program was thus 10,000.

The geometry of the poroelastic solid was assumed to be circular with one elastic solid inside the circle and another elastic material outside the circle. The radius of the circle was taken to be 30 mm. The PML layers on the left and right each occupied 10 grid points creating a total of 20 mm. Thus, along the horizontal axis of the geometry from the far left, there are consecutively: 10 mm of CPML, 10 mm of an elastic material, 60 mm of another elastic material (iron in this case), 10 mm of the elastic material again, and finally 10 mm of the CPML, as shown in Figure 20.

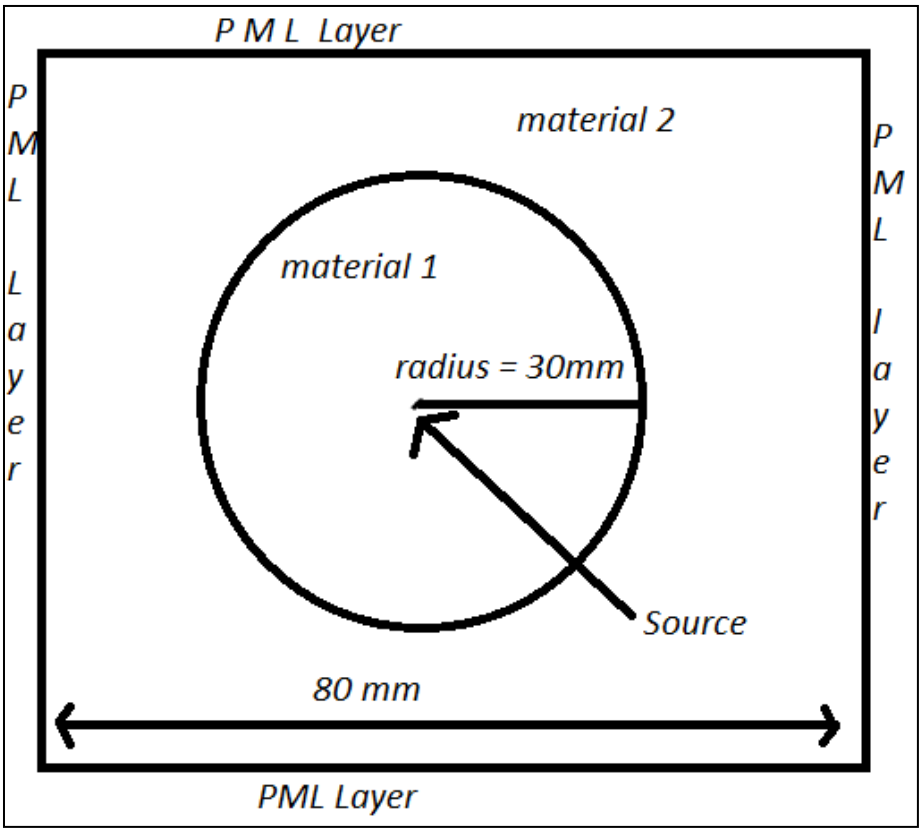

Figure 20 Geometry of the FDTD grid used for the elastic solids

3.2.2 Parameters

The elastic material inside the circle was assumed to be iron. The elastic material outside the circle was assumed to be mud that was slightly less denser than iron. The following are the parameters for the two materials used in the simulation.

Inside the circle the values were 5,956 m/s for c_p; 3,227.07 m/s for c_s; and 0.007874 kg m/s^2 for density. Outside the circle the values were 500000 for c_p; 1,000,000 for c_s; and 0.002000 kg m/s^2 for density.

3.2.3 Courant Number

It was taken care that the value of the Courant number was not above 1 or else the simulation would turn out to be unstable. Substituting, respectively, the values of *dx*, *dy*, *dt*, and *cp*, with 5956000 mm/sec, 10^{-8} sec, 1mm, and 1 mm, the Courant number was obtained to be 0.168, which is within the stability value of 1.

3.2.4 Source Location, Type, and Values

The source was located in the middle of the circle. Thus, the co-ordinate of *x* was 50mm, and the co-ordinate of *y* was 50mm. Its location can be changed very easily anywhere in the geometry. As in the two-dimensional poroelastic case, three different types of sources were used: Gaussian, first derivative of a Gaussian, and second derivative of a Gaussian.

The frequency of the source was taken to be 80 KHz. The amplification factor of the source was taken to be 100. It was time shifted for better clarity of the output graphs. An angle source of 90 degrees was used in this case. Taking source angles that deviated away from the receivers vastly led to very sharp wave patterns, while source angles that

aligned with the receivers produced smooth wave patterns. Here, the wavelength was obtained as 70.6 mm, which is larger than the size of the cell, which is 1 mm.

3.2.5 CPML Values

The CPML layers were implemented on all four sides of the grid. Equations used to calculate the values of CPML were same as the two-dimensional poroelastic case.

3.2.6 Type of FDTD Used

A staggered spatial finite difference grid was used. The positions of the discrete solid stresses and velocity in the solid are shown in Figure 21.

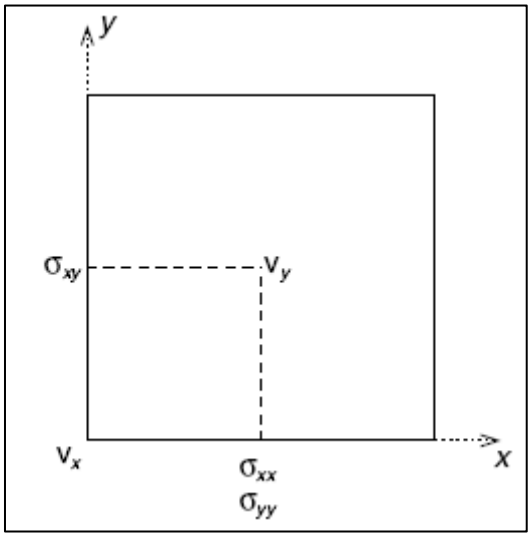

Figure 21 FDTD two-dimensional grid used for computation

3.2.7 Dirichlets Condition

On the external edges of the grid, i.e., at the top of each PML, a Dirichlet's condition was imposed on the velocity vector for the whole duration of the simulation. This gave v=0 for all t.

3.2.8 Image Plot

The variables were plotted using the same methods used in the poroelastic wave equations.

3.2.9 Receivers

As in the two-dimensional poroelastic case, the receivers that output the graph of the velocity and pressure were taken to be on top of the source and at the edge of the circle. So there were two receivers in the geometry. Their co-ordinates were (50 mm, 50 mm) and (25mm, 50mm). Each of them could be placed at any desirable position, but the given two locations were chosen for their ease of visualization. The values recorded from the receivers were velocity of the solid, velocity of the fluid, pressure, and stress in the solid. Figure 22 shows the location of the receivers with respect to the geometry of the two-dimensional material.

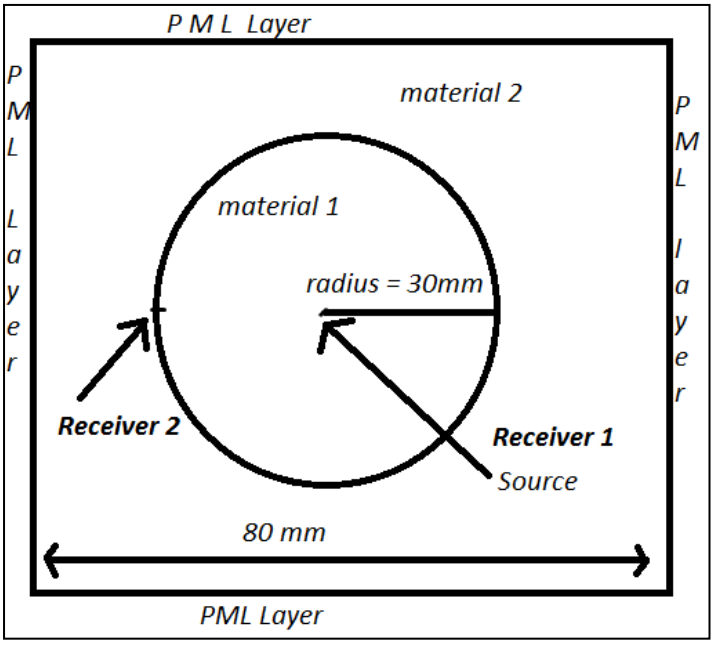

Figure 22 Geometry of the elastic solid showing the location of the receivers

3.2.10 Results Obtained When the Source is Located at Center (x=50mm, y=50mm)

Velocity in the solid, stress in the solid, pressure in the fluid, and velocity in the fluid are the variables whose graphs were obtained from the computations. However, only the graph of the solid velocity contained valuable information. So only the solid velocity graphs will be presented here in Figures 23, 24, and 25. The force applied to the materials in Figure 23, 24, and 25 are, respectively, a Gaussian source, the first derivative of a Gaussian source, and the second derivative of a Gaussian source.

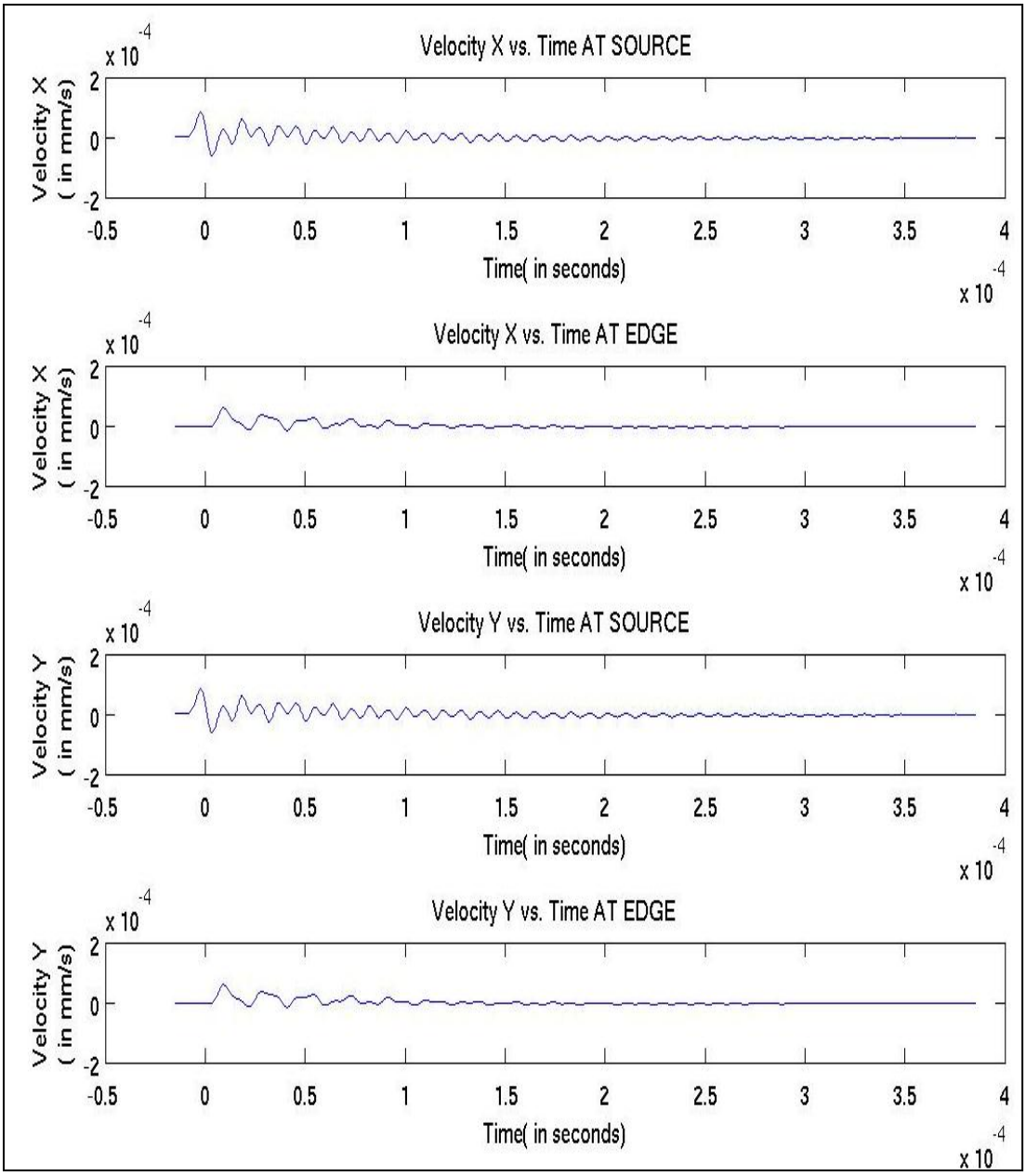

Figure 23 Velocity plots for source type of first derivative of Gaussian

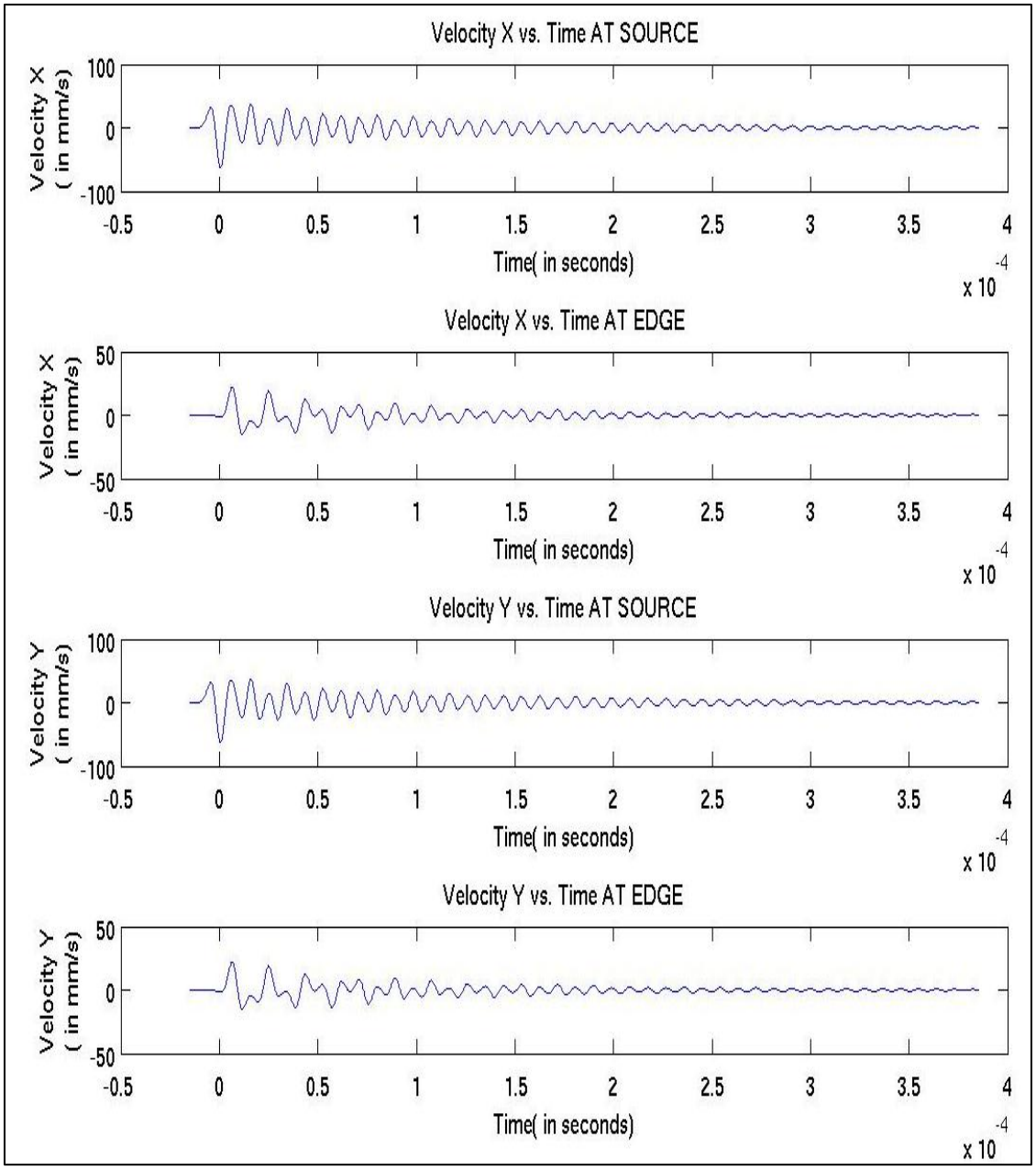

Figure 24 Velocity plots for source type of first derivative of Gaussian

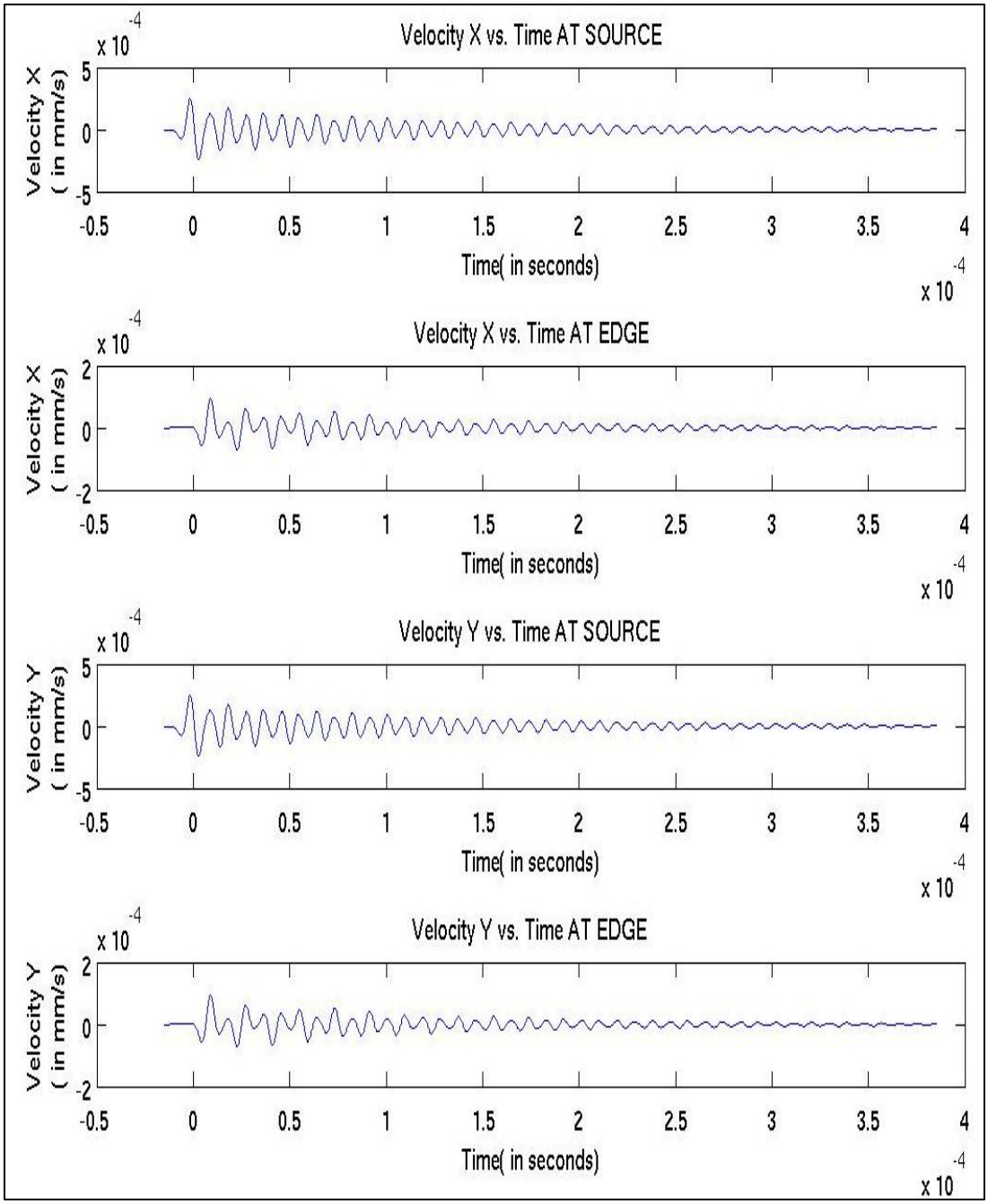

Figure 25 Velocity plot for source type of second derivative of a Gaussian

3.2.11 Analysis of the Speed of Wave in the Poroelastic Solid

From Figures 23, 24, and 25, it can be analyzed that the velocity of the wave is a different variable from the velocity of the particle that is being displaced in the material. The length of the elastic material considered was 60mm. From Figure 23, the time difference between the first wave peaks that transmitted from the source and then was received back at the source was 11.42 * 10^{-6} s. So the velocity was calculated, as shwon in Equation 3.8.

$$velocity = \frac{60mm}{11.42*10^{-6}} = 5.2539 * 10^{6}\ mm/\text{s} = 5253.9\ m/\text{s}\ . \qquad (3.8)$$

This value matches the value that was originally entered into the program, which was 5956 m/s with an accuracy of 11%. This small discrepancy was actually due to the grid size which, when taken smaller, would give a more accurate value. Thus, it was verified that the FDTD – CPML technique did simulate the wave equation propagation in poroelastic solids to an accuracy of 11%.

CHAPTER 4

CONCLUSION

Biot's theory and the FDTD technique were extensively used in this research project. The tensor representation of Biot's theory was expanded into partial differential equations so that FDTD calculations could be used on the PDE's.

FDTD is the standard method to solve partial differential equations involving time. So the simulation of wave equations is particularly well suited for FDTD solutions. To solve the boundary conditions in PDE, various absorbing boundary conditions are used that try to minimize the reflections from finite truncated domains. Mur ABC, Laio ABC, and Berengers PML, and Convolutional PML are some of the techniques.

Only a few theories have been formulated to explain the dynamics of poroelastic materials. The Biot and Hickey models or their variants are most commonly used. The amplitude of waves is not changed significantly by the Hickey model. The Hickey model includes factors for thermo mechanical coupling, porosity, and mass-density perturbations when the material is subjected to local pressure variations. In spite of these additions and improvements to the Biot's model by C.J. Hickey, Biot's model and Hickey's model lead to similar results and waveforms [6].

Various components of the two-dimensional wave velocity in the porous model correspond to a small square with CPML conditions implemented on the four sides.

There were time versus velocity plot for a particular position and also position versus velocity plot for a particular instant of time. These graphs were analyzed by color coding the amplitude of the velocity waves.

This project is a small part of a larger project, the ultimate long term goal of which was to contribute to the development of software which will simulate as realistically as possible the propagation of waves through various elastic, viscoelastic, and poroelastic materials with two-dimensional geometry and three-dimensional geometry. The objective of the research project conducted by us was to develop software that can simulate a two-dimensional model of wave propagation through elastic and poroelastic materials.

The velocity, stress, and pressure were computed using FDTD – CPML technique in Matlab, using the equations of Biot for an isotropic homogenous poroelastic and elastic material. The velocity analyzed from the graphs matched the theoretical velocity to an accuracy of 10% to 11%. Thus the objectives of the project were met.

Future recommendations for this project include calculating the efficiency of the methods used in the project, which can be analyzed by comparing the results with analytical or experimental models. Future researchers may also analyze it by plotting graphs of total energy versus time of the PML formulations. If these graphs do not show a fast decrease in energy with time, then the hypothesis which says that two-dimensional modeling of CPML boundaries is more efficient than two-dimensional modeling of PML boundaries can be proven wrong.

Thus a software program that produces the data files and image plots of the velocity in the solid, the velocity in the fluid, the pressure in the fluid and the stress in the

solid was successfully engineered. The physics of solid and fluid mechanics, and computational method of FDTD and CPML were used to make this project successful, along with a slight mathematical knowledge of tensors.

BIBLIOGRAPHY

[1] K. Yee, "Numerical solution of initial boundary value problems involving Maxwell's equations in isotropic media," IEEE Transactions on Antennas and Propagation**,** vol. 14, pp. 302–307, 1966.

[2] A. Taflove, "Application of the finite-difference time-domain method to sinusoidal steady state electromagnetic penetration problems," IEEE Transactions on Electromagnetic Compatibility, vol. 22, pp. 191–202, 1980.

[3] A. Taflove and S. C. Hagness, Computational Electrodynamics: The Finite-Difference Time-Domain Method, 3rd ed., MA: Artech House Publishers, ISBN 1-58053-832-0, 2005.

[4] D. Komatitsch and R. Martin, "An unsplit convolutional Perfectly Matched Layer improved at grazing incidence for the seismic wave equation," Geophysics, vol. 72, no. 5, pp. 155-167, 2007.

[5] R. Martin and D. Komatitsch, "An unsplit convolutional perfectly matched layer technique improved at grazing incidence for the viscoelastic wave equation," Geophysical Journal International, vol. 179, no. 1, pp. 333-344, 2009.

[6] R. Martin, D. Komatitsch, and A. Ezziani, "An unsplit convolutional Perfectly Matched Layer improved at grazing incidence for seismic wave propagation in poroelastic media," Geophysics, vol. 73, no. 4, pp. T51-T61, 2008.

[7] R. Martin, D. Komatitsch, and S. D. Gedney, "A variational formulation of a stabilized unsplit convolutional perfectly matched layer for the isotropic or anisotropic seismic wave equation," Computer Modeling in Engineering and Sciences, vol. 37, no. 3, pp. 274-304, 2008.

[8] J. A. Roden and S. D. Gedney, "Convolution PML: An Efficient FDTD Implementation of the CFS - PML for Arbitrary Media," Microwave and Optical Technology Letters, vol. 27, no. 5, pp. 334-339, 2000.

[9] D. Appelo and G. Kreiss, "A new absorbing layer for elastic waves," Journal of computational physics, vol. 215, no. 2, pp. 642-660, 2006.

[10] A. Hosokawa, "Simulation of ultrasound propagation through bovine cancellous bone using elastic and Biot's finite-difference time-domain methods," Journal of Acoustic Society of America, vol. 118, no. 3, pp. 1782-1789, 2005.

[11] P. J. White, G. T. Clement, and K. Hynen, "Longitudinal and shear mode ultrasound propagation in human skull bone," Ultrasound in Medicine & Biology, vol. 32, no. 7, pp. 1085-1096, 2006.

[12] F. L. Teixeira and W. C. Chew, "On causality and dynamic stability of perfectly matched layers for FDTD simulations," IEEE Transactions on Microwave Theory and Techniques, vol. 47, pp. 775-785, 1999.

[13] S. D. Gedney, G. Liu, J. A. Roden, and A. Zhu, "Perfectly matched layer media with CFS for an unconditionally stable ADI-FDTD method," IEEE transactions on Antennae and propagation, vol. 49, pp. 1554-1559, 2002.

[14] S. D. Gedney, "An anisotropic perfectly matched layer-absorbing medium for the truncation of FDTD lattices," IEEE Transactions on Antennas and Propagation, vol. 44, pp. 1630-1639, 1996.

[15] F. L. Teixeira and W. C. Chew, "A general approach to extend Berenger's absorbing boundary condition to anisotropic and dispersive media," IEEE Transactions on Antennas and Propagation, vol. 46, pp. 1386-1387, 1998.

[16] F. L. Teixeira and W. C. Chew, "General closed-form PML constitutive tensors to match arbitrary anisotropic and dispersive linear media," IEEE Microwave and Guided Wave Letters, vol. 8, no. 6, pp. 223-225, 1998.

[17] W. C. Chew and W. H. Weedon, "A 3D Perfectly Matched Medium from Modified Maxwell's Equations with Stretched Coordinates," Microwave and Optical Technology Letters, vol. 7, no. 4, pp. 599-604, 1994.

[18] R. J. Luebbers and F. Hunsberger, "FDTD for Nth-Order Dispersive Media," IEEE Transactions on Antennas and Propagation, vol. 40, pp. 1297-1301, 1992.

[19] J. H. Beggs, R. J. Luebbers, K. S. Yee, and K. S. Kunz, "Finite-Difference Time-Domain Implementation of Surface Impedance Boundary-Conditions," IEEE Transactions on Antennas and Propagation, vol. 40, pp. 49-56, 1992.

[20] J. P. Berenger, "A perfectly matched layer for the absorption of electromagnetic waves," Journal of Computational Physics, vol. 114, pp. 195-200, 1994.

[21] S. D. Gedney, "Perfectly matched layer media for an unconditionally stable three-dimensional ADI-FDTD method", Microwave and guided wave letters, vol. 10, no. 7, pp. 261-263, 2002.

[22] J. P. Berenger, "Improved PML for the FDTD solution of wave-structure interaction problems," IEEE Transactions on Antennas and Propagation, vol. 45, pp. 466-473, 1997.

[23] J. P. Berenger, "An effective PML for the absorption of evanescent waves in waveguides," IEEE Microwave and Guided Wave Letters, vol. 8, pp. 188-190, 1998.

[24] J. P. Berenger, "Evanescent waves in PML's: Origin of the numerical reflection in wave structures interaction problems," IEEE Transactions on Antennas and Propagation, vol. 47, pp. 1497-1503, 1999.

[25] J. P. Berenger, "Perfectly matched layer for the FDTD solution of wave-structure interaction problems," IEEE Transactions on Antennas and Propagation, vol. 44, pp. 110-117, 1996.

[26] M. A. Biot, "General theory of three-dimensional consolidation," Journal of Applied Physics, vol. 12, pp. 155-164, 1941.

[27] M. A. Biot, "Theory of propagation of elastic waves in a fluid saturated porous solid. I Low frequency range", The Journal of the Acoustical Society of America, vol. 28, pp.168-178, 1956.

[28] M. A. Biot, "Theory of propagation of elastic waves in a fluid saturated porous solid. II Higher frequency range," The Journal of the Acoustical Society of America, vol. 28, pp.179-191, 1956.

[29] M. A. Biot and D. G. Willis, "The elastic coefficients of the theory of consolidation," Journal of Applied Mechanics, vol. 24, pp. 594-601, 1957.

[30] M. A. Biot, "Mechanics of deformation and acoustic propagation in porous media," Journal of Applied Physics, vol. 33, pp. 1482-1498, 1962.

[31] R. Madariaga, "Dynamics of an expanding circular fault," Bulletin of the Seismological Society of America, vol. 66, pp. 639–666, 1976.